Gondwana Research 30 (2016) 159–178

Contents lists available at ScienceDirect

Gondwana Research

journal homepage: www.elsevier.com/locate/gr

Geology and geochemistry of the Triassic Wenquan Mo deposit and Mo-mineralized granite in the Western Qinling Orogen, China

Xiao Xiong [a], Laimin Zhu [a,*], Guowei Zhang [a], Ben Li [b], Liang Qi [a,c], David Stevenson [b], Tao Yang [a], Fei Wang [a], Jun Zheng [a], Hang Jiang [a], Anlin Guo [a]

[a] State Key Laboratory of Continental Dynamics, Department of Geology, Northwest University, Xi'an 710069, China
[b] Centre for Exploration Targeting, ARC Centre of Excellence for Core to Crust Fluid Systems (CCFS), School of Earth and Environment, The University of Western Australia, 35 Stirling Highway, Crawley, WA 6009, Australia
[c] State Key Lab of Ore Deposit Geochemistry, Institute of Geochemistry, Chinese Academy of Science, Guiyang, China

ARTICLE INFO

Article history:
Received 15 January 2015
Received in revised form 14 September 2015
Accepted 25 September 2015
Available online 23 October 2015

Keywords:
Wenquan Mo deposit
Wenquan granite
MMEs
Zircon
Magmatic mixing
Triassic

ABSTRACT

The recently-discovered Wenquan porphyry Mo deposit hosted in the Wenquan granite of the West Qinling Orogen has been recognized as a product of the Indosinian metallogenesis. Three generations of mineral assemblage for the deposit are identified as follows: (1) quartz–biotite–K-feldspar; (2) quartz–sulfide and (3) sulfide–calcite. Geochemical study shows that the mafic microgranular enclaves (MMEs) in the ore-bearing Wenquan granite have lower SiO_2, and higher Mg# and Nb/Ta ratios than the host granite itself. Different from the granite which have zircon $\varepsilon_{Hf(t)}$ values of −3.6–3.0 and T_{DM2} of 1234–890 Ma, the MMEs are characterized by the $\varepsilon_{Hf(t)}$ values of −10.1–10.8 and T_{DM1} of 865–441 Ma. This can be interpreted to indicate a mixture origin of the Meso- and Neoproterozoic crust-derived component and Neoproterozoic SCLM-derived materials for the formation of the Wenquan granite, which played an essential role in the Mo mineralization. Comparative Pb isotopic data between ores and K-feldspar suggest that the Wenquan granitic magma originated from the middle-lower crust of the South China Block and the ore-forming materials were incorporated by hydrothermal fluid differentiated from the Triassic magmatic system, with minor contribution of sedimentary rocks. The $\delta^{34}S$ values of 5.0–11.7‰ with a pronounced mode at 5.0 to 6.1‰ for the ores probably represent the sulfur incorporation of a typical magmatic hydrothermal fluid contaminated by heavy sulfur of Devonian sediments. The granite yielded the zircon U–Pb ages of 218 ± 2.4 Ma and 221 ± 1.3 Ma, as the same as the ages of 217 ± 2.0 Ma and 218 ± 2.5 Ma obtained for the MMEs. These ages are indistinguishable with the molybdenite Re–Os isochron age of 219 ± 5.2 Ma which is the timing for the Mo mineralization. Tectonically, the magmatic mixture processes of the Wenquan granite and the Mo mineralization to form the Wenquan Mo deposit contemporaneously occurred during the transition of tectonic regime from syn- to post-collision orogeny in the Qinling Orogen in the Late Triassic.

1. Introduction

The Qinling Orogen situated in central China marks the tectonic boundary between the South China Block (SCB) and the North China Block (NCB). The orogen connects with the Dabie–Sulu Orogen to its east and the Kunlun Orogen to the west (Zhang et al., 1995; Li et al., 1996; Meng and Zhang, 1999; Zhang et al., 2001; Ratschbacher et al., 2003; Dong et al., 2011a,b, 2013; Zheng et al., 2013; Dong and Santosh, 2015). The closure processes of the eastern paleo-Tethys branch and amalgamation between the South China and North China Blocks have formed widely-distributed Indosinian granitoids and related mineralization systems (Hu et al., 1988; Zhang et al., 2001; Sun et al., 2002; B.R. Zhang et al., 2002; Qin et al., 2009; Chen, 2010; Jiang et al., 2010; Qin et al., 2010; Zhu et al., 2010, 2011, 2013; Chen and Santosh, 2014; Chen et al., 2014). However, the importance of the Indosinian mineralization in the Qinling Orogen has not been recognized until recently a number of Triassic Au, Pb–Zn ± Ag, Au–Mo and Mo ore deposits were found. In fact, the Indosinian period represents an important metallogenesis era with significant metal endowment in the Qinling Orogen (Chen and Santosh, 2014, and references therein).

The newly-found Wenquan porphyry Mo deposit hosted in the Wenquan granite in the West Qinling Orogen (WQO), China, is another breakthrough for the Indosinian prospecting. For a long time, most studies have mainly focused on the timing and magma source of the Wenquan granite (Cao et al., 2011; Zhu et al., 2011) and ignored exploring the mafic microgranular enclaves (MMEs) (see below) present in the pluton. Actually, a study on MMEs can provide critical information in the understanding of the source materials, generation of granitic melt and crust–mantle interaction (Vernon, 1984; Vernon et al., 1988; Didier and Barbarin, 1991; Wiebe et al., 1997; Perugini et al., 2003, 2004; Yang et al., 2006, 2007; Qin et al., 2009, 2010; Zhu et al., 2013).

* Corresponding author. Tel.: +86 13772547955.
E-mail address: zhulaimin@nwu.edu.cn (L. Zhu).

http://dx.doi.org/10.1016/j.gr.2015.09.013
1342-937X/

In addition, more and more researches have suggested that hybrid magma with input of mantle-derived hydrous melt plays an essential role in generating porphyries and related ore deposits (Keith et al., 1997; Maughan et al., 2002; Ma and Chen, 2011; Ma et al., 2013), and in porphyry Cu–Mo deposit systems, sulfur and metals are transferred in a rather direct fashion from mafic to felsic magma as a result of magma mixing (Keith et al., 1997; Hattori and Keith, 2001; Halter et al., 2002; Audetat and Pettke, 2006; Stern et al., 2007). Therefore, the study focusing on MMEs for the Wenquan granite becomes needed in order to better understand the origin of granitic magma and constrain the material source of the Mo mineralization.

In this paper, we report in situ zircon U–Pb dating results and Hf isotopic data of the MMEs and host granite, and major and trace element geochemistry of the MMEs. Combining with molybdenite Re–Os geochronological and mineral Pb and S isotopic studies, we attempt to explore the magma source of the MMEs and granite as well as possible magma mixing processes for constraining the genesis and geodynamic setting of the Wenquan granite and Mo mineralization.

2. Regional geology

The Qinling Orogen, as a major portion of the Central Orogenic Belt of China has experienced prolonged and multiphased tectonic evolution and represents a typical continental composite orogen (Zhang et al., 2001). The present Qinling orogen appears in a tectonic framework of "three-plate with two suture zone" (Fig. 1). From north to south, there are the following tectonic units: the southern margin of the North China Block (NCB), the former suture zone now the Shangdan Tectonic Zone, the South Qinling Belt (SQB), the former suture zone now the Mianlue Tectonic Zone and the northern margin of the Yangtze Block (Meng and Zhang, 1999; Zhang et al., 2001; Dong et al., 2011a,b). The Shangdan suture zone is generally considered to be formed following subduction of the Shangdan Ocean and multistage amalgamation of the South Qinling to the NCB. The suture underwent the Middle Paleozoic subduction–collision event and Mesozoic–Cenozoic intraplate strike-slip faulting (Zhang et al., 2001; Ratschbacher et al., 2003; Zhang et al., 2004), forming the Linxia–Wushan–Tianshui fault with a variable width of 1–10 km in a different section (Fig. 1) (Dong et al., 2008) and a number of outcrops of ophiolitic melanges and arc-related volcanic rocks (Dong et al., 2011b). From west to east, the ophiolite melanges are mainly exposed in the Yuanyangzhen, Wushan, Guanzishan, Tangzang, Yanwan, Heihe and Danfeng areas (Zhang et al., 2001; Dong et al., 2011b, 2012). To the north of the Shangdan fault, there is the North Qinling Belt (NQB), which is separated from the northern margin of the NCB by the Luonan–Luanchuan–Fangcheng fault. As part of the trench–arc–basin tectonic system formed by northward subduction of the Paleo-Qinling ocean along the Shangdan suture in the early Paleozoic, the NQB is a composite tectonic belt, which was subsequently overprinted by the intracontinental orogenesis after the late Triassic closure of the Mianlue Ocean. All the tectonic units such as the Kuanping, Erlangping, and Qinling Groups, and the Songshugou Proterozoic ophiolite are separated by thrust faults or ductile shear zones (Zhang et al., 2001; Dong et al., 2011a, 2012). To the south of the Shangdan suture zone, the SQB is characterized by a pre-Sinian basement with overlying Sinian and Phanerozoic sedimentary rocks which have undergone thin-skinned deformation (Zhang et al., 2001). There are large amounts of Triassic granitoids intruded the western SQB as results of the subduction and collision between the South Qinling micro-block and SCB along the Mianlue suture (Zhang et al., 2001; Qin et al., 2009; Chen and Santosh, 2014; Li et al., 2015). The Mianlue suture zone represents the closure of a northern branch of the eastern Paleo-Tethyan Ocean that separated the South Qinling micro-block from the South China Block (SCB) (Zhang et al., 1995; Li et al., 1996; Zhang et al., 2000; Dong et al., 2011a, 2012). Ophiolites, oceanic island and island-arc volcanic rocks crop out in the Mianlue suture zone (Zhang et al., 2001, 2004; Dong and Santosh, 2015).

The WQO, separated from the East Qinling Orogen by the Mesozoic Huixian–Chengxian basin, is bounded by the Tangzang–Wushan–Linxia–Guide fault to the north and the Mianlue suture to the south (Fig. 1). Along with these two boundary faults, the WQO lies adjacent

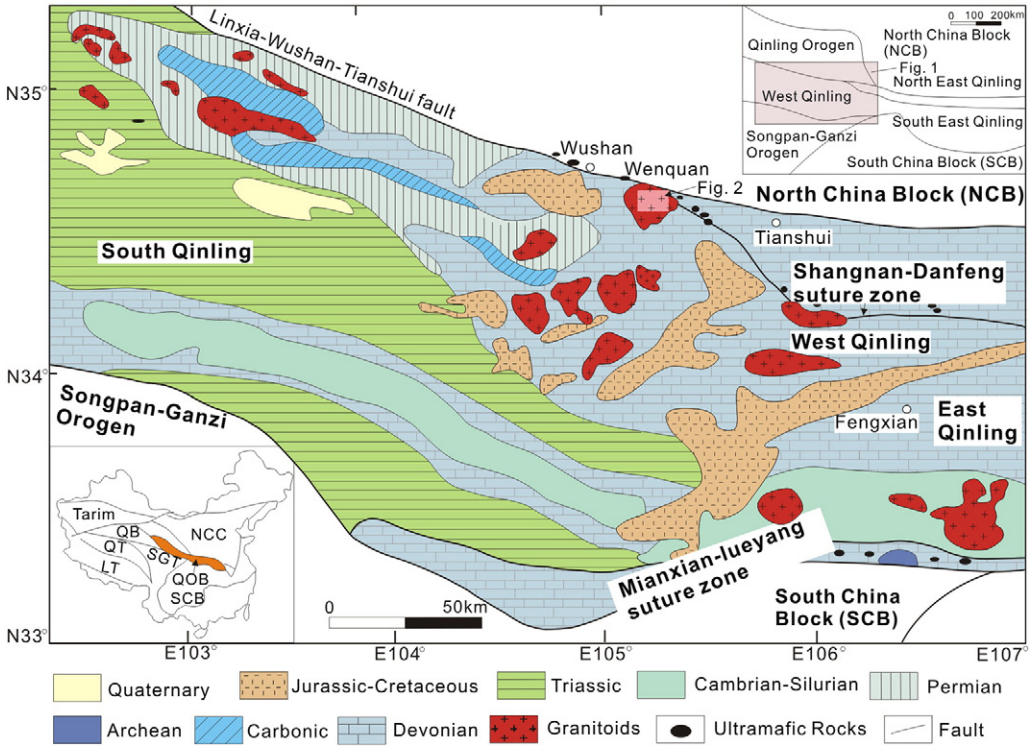

Fig. 1. Regional geological sketch map of the West Qinling Orogen.
Modified after Cao et al. (2011).

to the Qilian Orogen to the north and the Bayan Har–Songpan Orogen and Bikou terrane to the south, respectively (Zhang et al., 2001; Feng et al, 2002; Zhang et al, 2007; Zhu et al., 2009). The exposed strata are dominated by the Sinian to middle Triassic sedimentary rocks. Structural deformation in the strata records the continent–continent collision of the Qinling Orogen (Zhang et al., 2001). Approximately 200 Triassic granitic plutons were intruded throughout the WQO, with an individual area varying from less than 1 km^2 to 500 km^2 and a total area of 4000 km^2 (X.Z. Li et al., 1993; J. Zhang et al., 2002; Li et al., 2003a; Zhang et al., 2007; Q. Zhang et al., 2009). Most granitic plutons in E–W trending are distributed in the region (in the areas such as the Guangtoushan, Mishuling, Miba, Tianzishan, Wenquan, Zhongchuan, Jiaochangba, Luchuba, Jiangwu, and Daerzang) between the Shangdan and Mianlue sutures and have the MMEs contained (Li et al., 2003b; Gong et al., 2009a; Q. Zhang et al., 2009; Qin et al., 2009; Zhu et al., 2009,; Yang et al., 2013; Zhu et al., 2013,; Zeng et al., 2014).

3. Geology of the Wenquan Mo deposit

3.1. Structure framework

The Wenquan Mo deposit is located at the southern side of the Shangdan suture. It's within the conjunct zone among the WQO, the North Qinling Orogen and the Qilian Orogen. Geographically, it sits near Wushan County, Gansu province, China. The deposit is constraint by the Linxia–Wushan–Tianshui fault to the north, and by Wushan–Niangniangshan fault to the south (Fig. 1). The structures developed in Wenquan Mo deposit such as faults and joint fissures control the distribution of Mo orebodies. The fault structure in the deposit is mainly N–S, N-E and N-W striking, forming a series of parallel faults with intensive rock fragmentation (Fig. 2). Breccias commonly occur in some large-scale fault zones, with molybdenite veinlets filling in the fissures. In the Wenquan Mo deposit, the joint structures, especially the shear joints marked by straight joint plane and far-extension are also developed. The joints are characterized by multistage cross cutting, which form stockworks. The striking and dipping of the primary joints can be subdivided into four groups (Ren, 2009): (1) striking 10° to 350°, dipping 45° to 80° to EW; (2) striking 30° to 60°, dipping 45° to 75° to NW; (3) striking 300° to 340°, dipping 45° to 80° to NE; and (4) striking 80° to 95°, dipping 65° to 80° to N or E. The second and third groups are the most commonly seen joints, which are filled with smoky gray to charcoal gray molybdenite-bearing quartz.

3.2. Orebodies and mineralogy

The Wenquan Mo deposit is hosted by the Wenquan granitic complex (Figs. 2 and 3). There are 4 mineralization belts, 42 Mo mineralization zones and 34 orebodies with Mo grade ranging from 0.03% to 3.99% (averaging at 0.05%). The contents of ore-forming elements such as Mo, Cu, Ag and As are 2 to 7 times higher than the adjacent areas (Zhou and Han, 2010). Orebodies are stratiform and irregular vein shaped with 340° to 355° striking and 30° to 75° dipping, and integrated in deep (Fig. 3) (Ren, 2009). The faults and the primary joints in the pluton strictly control the orebodies. Molybdenite–quartz veins fill in the altered tectonic zone and primary joints (Fig. 5a).

Metallic minerals are mainly composed of molybdenite, pyrite, chalcopyrite, as well as minor bornite, tetrahedrite and galena. Gangue minerals include quartz, calcite, K-feldspar, plagioclase, biotite, sericite, chlorite, epidote, apatite and chalcedony. Supergene minerals are chalcocite, covellite, malachite and limonite. Molybdenite is the major ore-forming mineral, which distributes in quartz veins or disseminates in the potassic-altered granites. Textures of molybdenite from the Wenquan Mo deposit include: (1) flake, scaly, polysynthetic and lath-shaped texture (Fig. 4e); (2) radiated or massive aggregation (Fig. 4b); (3) subhedral to euhedral granular texture associated with chalcopyrite and pyrite (Fig. 4f); and (4) replaced by chalcopyrite with metasomatic texture (Fig. 4e). Chalcopyrite, pyrite, galena and sphalerite are granular grains and aggregation. Molybdenite is present in the forms of films,

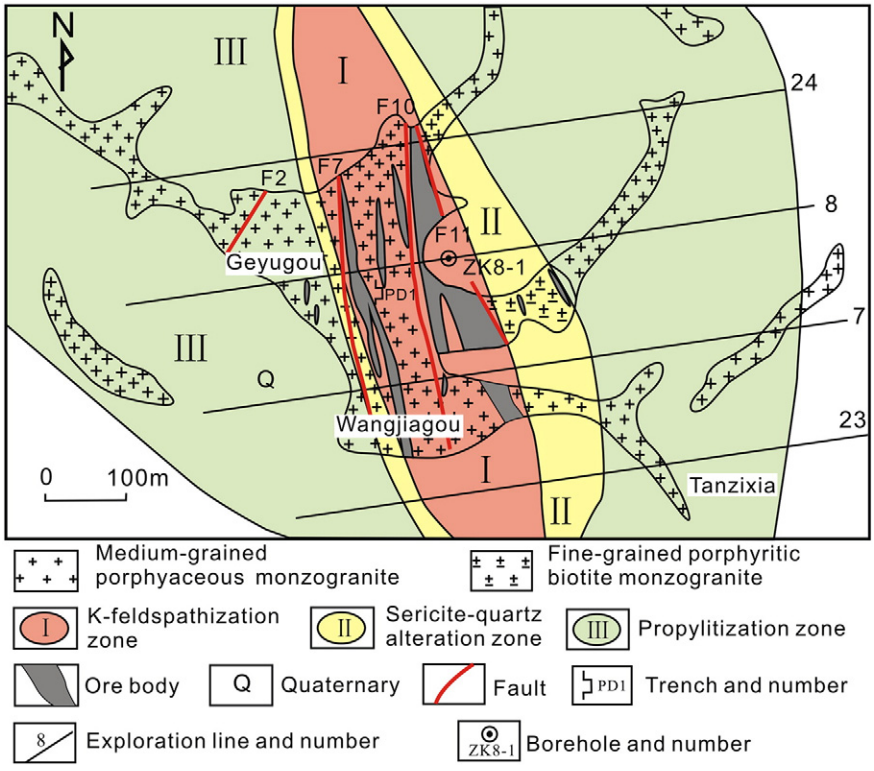

Fig. 2. Zonations of wall–rock alteration of the Wenquan Mo deposit.
After Qiu et al. (2014).

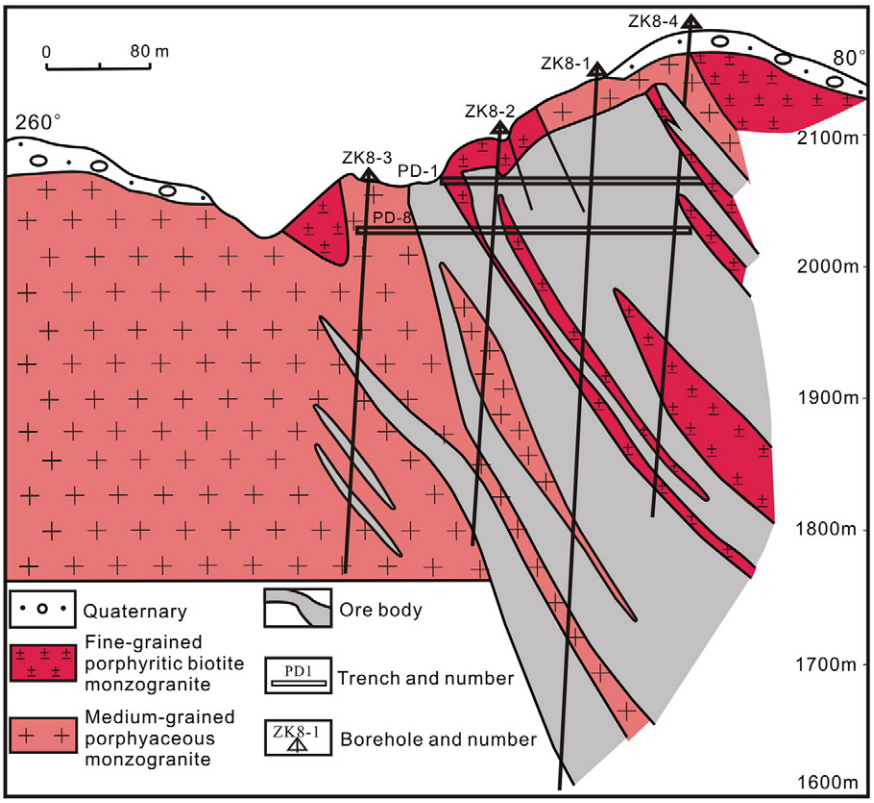

Fig. 3. Geological profile map along No. 8 prospecting line from the Wenquan Mo deposit. Modified after Wang et al. (2012).

disseminated spots, or in stockworks and veinlets. Fine-grained pyrite and chalcopyrite are dispersed in gangue minerals.

3.3. Vein paragenesis

Based on cross cutting relationships and mineral paragenesis, veins in the Wenquan Mo deposit can be subdivided into: (1) quartz–biotite–K-feldspar veins; (2) quartz–sulfide veins and (3) sulfide–calcite veins. The quartz–biotite–K-feldspar veins feature replacement of plagioclase and orthoclase by quartz and K-feldspar. Hydrothermal quartz–K-feldspar veins developed in this stage are commonly present with sulfides, such as pyrite, chalcopyrite and minor molybdenite (Fig. 4a, c). The quartz–sulfide veins are the principal Mo-host veins (Fig. 4b), which are dominated by various sulfide associations with molybdenite, pyrite, chalcopyrite, bornite, tetrahedrite, galena and sphalerite. The sulfide–calcite veins have the similar sulfide associations with the quartz–

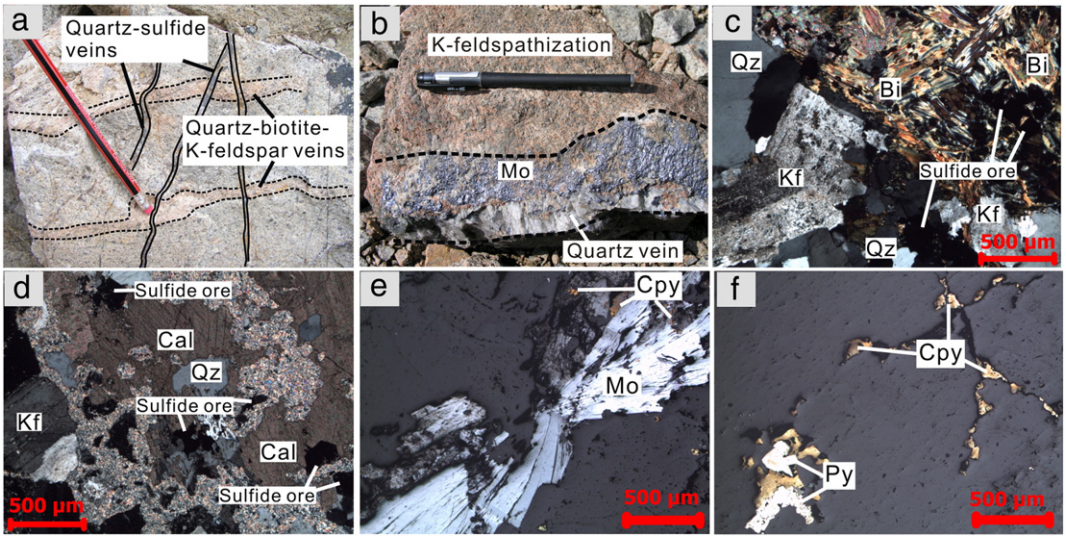

Fig. 4. Representative field and microscopic photographs of the Wenquan Mo deposit. (a) Interleaving ore-bearing quartz veins cut through the quartz–biotite–K-feldspar veins in the Wenquan pluton; (b) Mo-bearing veins with width of 8–10 cm in the K-feldspathization granite; (c) paragenesis of quartz–biotite–K-feldspar assemblage with a little sulfide; (d) sulfide–calcite association; (e) chalcopyrite disseminates in radiated molybdenite aggregation; (f) anhedral–subhedral pyrite and chalcopyrite assemblage in quartz. Mo — molybdenite; Cpy — chalcopyrite; Py — pyrite; Kf — K-feldspar; Qz — quartz; Bi — biotite; Cal — calcite.

sulfide veins, but they have more calcite, less quartz, molybdenite and other sulfides (Fig. 4d). Supergene minerals include chalcocite, covellite, limonite and malachite.

3.4. Wall rock alteration

Alterations of wall rocks in the Wenquan Mo deposit are complex and intensive, including K-feldspathization, silicification, zeolitization, sericitization, kaolinization, chloritization, epidotization, malachitization and carbonatization. Among them, silicification and zeolitization is the most common. From the interior to the exterior of the deposit alteration can be divided into the K-feldspathization, the quartz–sericite and the propylitization alteration zones (Fig. 2) (Qiu et al., 2014). The K-feldspathization zone contains altered biotite, K-feldspar, quartz and sericite, with mineral associations dominated by molybdenite, chalcopyrite and minor pyrite and bornite. The sericite–quartz alteration zone mainly contains quartz and sericite, together with molybdenite, chalcopyrite, pyrite, bornite, sphalerite and galena. Molybdenite aggregations concentrate in the contacts between quartz veins and wall rocks. Orebodies are mainly distributed within the two zones above. The propylitization zone includes hydrothermal minerals such as chlorite, epidote, quartz and calcite, with pyrite and chalcopyrite.

4. Lithology of the host granite and MMEs

The Wenquan Mo deposit hosted by the Wenquan granitic pluton is located in Simen–Wenquan Town. The northeast side of the Wenquan pluton intruded the Lower Paleozoic Liziyuan Group, which has the lithologies of plagioclase amphibole schist, marble, epidote–chlorite schist, sericite–quartz schist, biotite–quartz schist and calcareous schist. The south side of the pluton intruded the clastic sedimentary rocks of Upper Devonian Dacaotan Group (Fig. 1).

The ore-bearing granites are composed of the following subtypes:

The medium-grained porphyaceous monzogranite which commonly contains the MMEs is the main rock type of the Wenquan complex (Fig. 5b, c). It is gray-pale red color with porphyaceous texture (Fig. 5f). The phenocrysts are euhedral lath-shaped K-feldspar sized at 15 to 30 mm, and account for a 5 to 10% in volume of the pluton. Carlsbad twins, plagioclase and biotite inclusions can be observed in the phenocrysts. The matrix consists of 30 to 35% K-feldspar, 30 to 35% plagioclase, 25 to 30% Quartz, 3 to 8% biotite, 2 to 4% hornblende and accessory minerals (including euhedral short-column or acicular apatite, sphene, zircon and magnetite). K-feldspar in matrix commonly shows perthitic texture with rare grid twin, while plagioclase has polysynthetic twin and Carlsbad-albite compound twin with sericitization and kaolinization (Fig. 5f). Quartz commonly replaces K-feldspar and shows metasomatic perforation texture and myrmekitic texture.

Fine-grained porphyritic biotite monzogranite is in light-gray and pale red color (Fig. 5e). The phenocryst is composed of K-feldspar (5 to 13%) and plagioclase (5 to 15%). The proportion of K-feldspar phenocryst is much less than that in the medium-grained porphyaceous monzogranite. The matrix consists of K-feldspar (20 to 30%), plagioclase (15 to 25%), quartz (15 to 25%), biotite (2 to 3%) and hornblende.

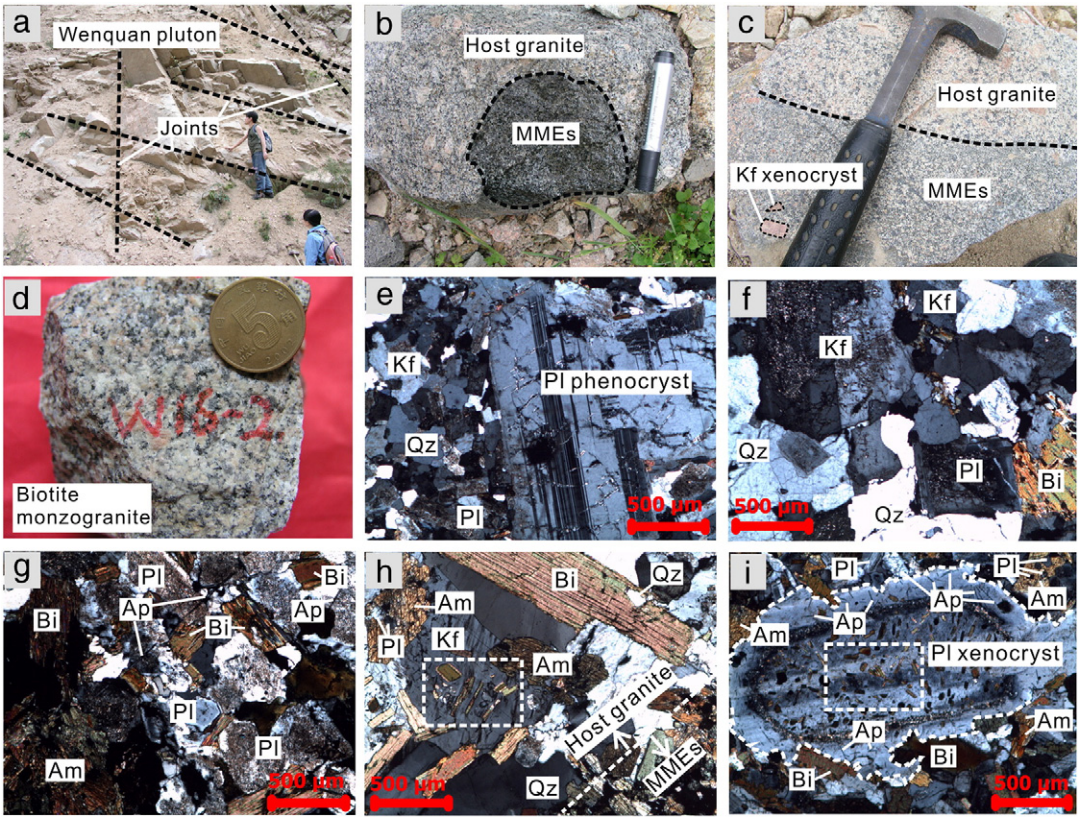

Fig. 5. Representative field and petrographic characteristics of the host granite and enclosed MMEs from the Wenquan pluton. (a) Ore-bearing quartz veins fill in the joint fissures of the granitoids; (b) and (c) rounded and angular MMEs in the granite with sharp chilled margin, contain K-feldspar and plagioclase xenocryst; (d) biotite monzogranite with fine-grain equigranular texture and massive structure; (e) the granite (fine-grained porphyritic biotite monzogranite); (f) the granite (medium-grained porphyaceous monzogranite); (g) the MMEs which are diorite and have igneous microtexture, comprise of plagioclase with saussuritization, amphibole, biotite and minor acicular apatite; (h) lopsided mineral textures occur in contacted zone between the granite (left upper) and MMEs (right lower): euhedral biotite and amphibole wrapping the anhedral quartz and feldspar inclusions, feldspars wrapping the micro-crystallites of biotite, amphibole and feldspar from another generation (in white dotted box); (i) plagioclase xenocryst with abnormal zoning in the MMEs is corroded and showing harbor or sawtooth texture. Acicular apatite and micro-crystallites can be observed. Kf — K-feldspar; Pl — plagioclase; Qz — quartz; Bi — biotite; Am — amphibole; Ap — apatite.

K-feldspar phenocrysts are locally replaced by quartz, which has metasomatic perforation texture and myrmekitic texture. Accessory phases include sphene, apatite and zircon.

Fine-grained biotite monzogranite is pale-red in color (Fig. 5d). It consists of K-feldspar (30 to 35%), plagioclase (30 to 35%), quartz (25 to 30%) and biotite (3 to 5%). Accessory minerals include apatite, sphene, zircon and primary pyrite. Mineralization in this granite is not as extensive as that in the medium-grained porphyaceous monzogranite and Fine-grained porphyritic biotite monzogranite.

The MMEs are hosted by the medium-grained porphyaceous monzogranite in ellipsoid, subrounded or irregular shapes (Fig. 5b, c). The contact boundaries between the MMEs and the host granite are vague. The MMEs are mostly dioritic with mineral composition of plagioclase (55 to 60%), hornblende (30 to 35%), K-feldspar (5 to 10%), biotite (<3%), quartz (<3%) and very rare pyroxene (Fig. 5g). Accessory phases include sphene, zircon and apatite. The plagioclase is subhedral–euhedral. Polysynthetic twin and zoning texture are observed in the plagioclase. The contact between plagioclase and K-feldspar often forms Carlsbad-albite compound twin with myrmekitic texture. Hornblende is subhedral–euhedral. Biotite crystals are present between the intervals or enclosed by other minerals (Fig. 5g). Apatite in the MMEs is acicular and has a larger proportion than the granite (Fig. 5g, i). Some of the MMEs contain plagioclase and K-feldspar xenocrysts of the granite (Fig. 5c, i). Some xenocrysts transect crenulated boundaries between granite and MMEs or enter MMEs (Fig. 5c). The xenocrysts are corroded and showing harbor texture (Fig. 5i). The above indicates that there has been an exchange of material composition between the granite and MMEs.

5. Samples and analytical methods

5.1. Major and trace element analyses

The least altered samples of MMEs from the Wenquan pluton were separated from the host granite for whole-rock major and trace element analyses. Ten samples were cut, crushed and milled. A major element analysis was done at the Key Laboratory of Continental Dynamics of Northwest University, Xi'an, China. Major oxides were analyzed using X-ray fluorescence (RIX2100X sequential spectrometer) on fused Li-borate glass beads, with BCR-2 and GBW07105 as reference materials. Both of the relative precision and accuracy were within 5%. Trace elements, including REEs, were analyzed using a Finnigan Element ICP-MS at the Institute of Geochemistry, Chinese Academy of Sciences, Guiyang, China, following the procedures described in Qi et al. (2000) with an analytical precision of ±5 to 10%.

5.2. Zircon LA-ICP-MS U–Pb age dating and Lu–Hf isotopes

Zircons separated from the host granite (samples W3-1 and W9-1) and MMEs (samples W23-1 and HGL-2) were mounted for in situ U–Pb dating and Lu–Hf isotopic analysis. Zircon separation including heavy liquid and magnetic separation methods were conducted at the Institute of Geophysics and Geochemistry, Ministry of Land and Resources, Langfang, China. Zircon concentrates were handpicked under a binocular microscope, mounted in epoxy resin and polished to expose the grain interiors. Prior to analysis, the mount surfaces were cleaned using 3% HNO_3 to remove any lead contamination. Cathodoluminescence (CL) images were obtained using a Quanta 400 FEG scanning electron microscope from FEI (USA8) equipped with a Mono CL3 + cathodoluminescence spectroscope produced by Gatan Corporation (USA). In situ zircon analyses were conducted at the State Key Laboratory of Continental Dynamics, Northwest University, Xi'an, China. Zircon U–Pb ages were obtained using a GeoLas 2005 Laser Ablation (Coherent, USA) coupled with an Agilent 7500a ICP-MS and Lu–Hf isotopic compositions were obtained using the same laser system coupled with a Nu Plasma HR (Wrexham, UK) MC-ICP-MS. A 50 mJ/pulse (Geolas) 193 nm ArF Excimer (Lambda Physik, Göttingen Germany) laser was used to ablate the zircons at 10 Hz. The diameter of the laser ablation spot was 32 μm. Helium was used as a carrier gas to transport the ablated aerosol from the laser-ablation cell to the ICP-MS torch. U–Pb ages showing any detectable common Pb (from the ^{204}Pb count rate) were neglected. The detailed analytical procedures used follow those described by Yuan et al. (2004). Harvard zircon 91500 was used as an external standard to normalize isotopic fractionation during analysis (Wiedenbeck et al., 2004). The NIST SRM610 glass was used as an external standard to calculate U, Th, and Pb concentrations of unknowns. Raw data were processed using GLITTER (version 4.4) (Jackson et al., 2004). Common Pb correction was applied using the method of Andersen (2002). Uncertainties of individual analyses are reported with 1σ errors; weighted-mean ages were calculated at 2σ confidence level. The data were processed using ISOPLOT (version 3.0) (Ludwig, 2003). During this analysis the zircon standards 91500 and GJ-1 yielded weighted average $^{206}Pb/^{238}U$ ages of 1062 ± 5.6 Ma (2σ) and 605 ± 2.4 Ma (2σ) respectively, which were in good agreement with the referenced ages (Wiedenbeck and Griffin, 1995; Jackson et al., 2004).

The protocol used in the in situ Lu–Hf isotope analysis of zircon was after Yuan et al. (2008). The analyses were conducted with a 44 μm ablation spot size, with a laser energy of 50 mJ/pulse at 8 Hz. Interference of ^{176}Lu on ^{176}Hf was corrected by measuring the intensity of the interference-free ^{175}Lu, using the recommended $^{176}Lu/^{175}Lu$ ratio of 0.02669 (DeBievre and Taylor, 1993) to calculate $^{176}Lu/^{177}Hf$. Similarly, the isobaric interference of ^{176}Yb on ^{176}Hf was corrected by using a recommended $^{176}Yb/^{172}Yb$ ratio of 0.5886 (Chu et al., 2002) to calculate $^{176}Hf/^{177}Hf$ ratios. Zircon 91500 was used as the reference standard (Woodhead et al., 2004). The obtained $^{176}Hf/^{177}Hf$ ratio is 0.282296 ± 50 (2σ) for 91500 and 0.282019 ± 15 (2σ) for GJ-1, which is in good agreement with the recommended $^{176}Hf/^{177}Hf$ ratios of 0.2823075 ± 58 (2σ) for 91500 and 0.282015 ± 19 (2σ) for GJ-1 (Elhlou et al., 2006).

A decay constant for ^{176}Lu of 1.867×10^{-11} yr^{-1} was adopted after Söderlund et al., 2004. The initial $^{176}Hf/^{177}Hf$ ratio, denoted as $\varepsilon_{Hf(t)}$, is calculated relative to the chondritic reservoir with a $^{176}Hf/^{177}Hf$ ratio of 0.282772 and $^{176}Lu/^{177}Hf$ of 0.0332 (Blichert-Toft and Albaréde, 1997). Single-stage Hf model ages (T_{DM1}) are calculated relative to the depleted mantle with a present day $^{176}Hf/^{177}Hf$ ratio of 0.28325 and $^{176}Lu/^{177}Hf$ of 0.0384, and two-stage Hf model ages (T_{DM2}) are calculated by assuming a mean $^{176}Lu/^{177}Hf$ value of 0.0093 for the average upper continental crust (Vervoort and Blichert-Toft, 1999).

5.3. Re–Os dating

Five molybdenite samples were collected for Re–Os isotope dating from the molybdenite-bearing quartz stockworks and veinlets within the Wenquan granites. We crushed the samples and picked pure molybdenite under a binocular microscope. Re–Os isotope analysis was carried out on an ELAN DRC-e ICP-MS, in the State Key Lab of Ore Deposit Geochemistry, Institute of Geochemistry, Chinese Academy of Sciences, Guiyang. The sensitivity of the instrument was adjusted to ≥40,000 cps for 1 ng ml^{-1} of ^{115}In, and the relative standard deviation (RSD) was <3%. Analytical quality was controlled by the standard materials GBW04436 (JDC). Two measurements of JDC showed that the contents of Re and ^{187}Os and the model ages are consistent with the referenced values within error (A.D. Du et al., 2004), which confirms the accuracy and reliability of molybdenite Re–Os analysis from the Wenquan Mo deposit.

Detailed analytical procedures, including chemical separation of Re and Os and mass spectrometric determination were described by Qi et al. (2010). Samples, as well as appropriate volumes of Re and Os spikes were weighed and placed in Carius tube. After adding concentrated HCl and HNO_3, the sealed Carius tube was placed in a stainless steel jacket (as a precaution in the case of an explosive chain reaction) and heated to 200 °C for ~10 h. The Carius tube was allowed to cool at

room temperature prior to 2 h of refrigeration followed by distillation of Os in a boiling water bath. Periodic slow injections of H_2O_2 enabled oxidation of Os within the tube. OsO_4 was trapped within less than 1 ml water cooled in an ice-water bath for about 30 min. After distillation, the residual solution was transferred to a Savillex Teflon beaker and evaporated until completely dry two times using 5 ml concentrated HCl to remove the remaining HNO_3. The resultant solution was dissolved within 10 ml of 2 mol/L HCl with AG 1-X8 anion exchange resin to separate Re from the matrix.

5.4. Sulfur isotopes

Molybdenite and pyrite separated from different ore types were analyzed for sulfur isotopes. Samples were milled to 200-mesh. The

Table 1
Major (wt.%) and trace element (ppm) analyses of host granite and mafic enclaves.

Sample	Mafic microgranular enclaves										Host granite (n = 20)		
	W4-1	W4-2	W23-1	W23-3	HGL1-1	HGL1-2	HGL2-1	HGL2-2	HGL2-3	HGL2-4	Min	Max	Average
Major oxides (wt.%)													
SiO_2	60.3	60.5	58.0	58.9	53.6	57.3	52.9	53.3	53.72	53.2	69.7	73.2	71.81
TiO_2	0.68	0.67	0.87	0.82	0.84	0.56	1.20	1.17	1.15	1.16	0.15	0.69	0.34
Al_2O_3	13.6	13.6	15.0	14.8	12.6	13.3	16.8	16.7	16.5	16.7	12.7	15.1	14.0
TFe_2O_3	6.43	5.94	7.73	7.10	9.43	5.55	8.81	8.64	8.55	8.72	1.57	3.86	2.29
MnO	0.22	0.21	0.21	0.20	0.27	0.12	0.19	0.18	0.18	0.19	0.02	0.08	0.05
MgO	4.77	4.70	4.31	4.06	6.96	7.18	5.02	4.88	4.84	4.94	0.45	1.57	0.89
CaO	4.47	4.50	5.24	5.06	5.54	4.90	6.13	5.95	6.03	6.04	0.61	2.47	1.47
Na_2O	3.16	3.13	3.93	3.81	2.03	2.04	4.33	4.46	4.42	4.50	2.95	3.97	3.49
K_2O	4.76	5.05	3.33	3.60	5.49	6.90	2.84	2.45	2.34	2.34	3.52	5.18	4.68
P_2O_5	0.43	0.43	0.38	0.36	0.73	0.43	0.65	0.62	0.61	0.63	0.08	0.24	0.15
LOI	0.96	1.02	0.94	0.84	2.07	1.26	1.28	1.65	1.45	1.56	0.38	1.91	0.87
Total	99.7	99.7	99.9	99.5	99.5	99.5	100	100	99.8	99.9	99.5	100	100.03
A/CNK	0.73	0.72	0.77	0.77	0.65	0.67	0.79	0.80	0.79	0.80	0.97	1.23	1.04
A/NK	1.31	1.28	1.49	1.46	1.36	1.22	1.65	1.67	1.68	1.68	1.23	1.40	1.30
Mg#	63.4	64.8	56.5	57.1	63.2	75.1	57.1	56.8	56.9	56.9	40.1	56.3	46.7
Trace elements (ppm)													
Li	54.50	38.10	38.50	32.80	95	48.6	62.4	63.3	60.3	66.5	17.1	49.7	26.22
Be	5.82	4.76	9.09	7.59	5.93	5.47	9.5	9.55	9.93	9.35	2.63	5.85	4.53
Sc	16.30	13.50	26.80	21.40	24.7	16.4	24.6	23.1	25.2	24.8	2.67	6.14	4.28
V	104	100	130	126	158	111	145	142	146	150	14.2	44.3	26.15
Cr	278	283	109	118	547	452	69	66	68	68	18	65.2	34.34
Co	82.9	99.7	73.4	70.1	49.0	57.0	40.0	51.0	58.0	51.0	114	292	170
Ni	44.2	48.7	24.2	26.0	81.4	189	8.7	9.4	10.0	9.1	10.2	32.4	16.4
Cu	46.8	60.8	254	349	23.7	16.6	59.1	48.8	48.5	46.6	4.08	722	234.18
Zn	144	140	162	150	204	92	170	197	173	174	37.7	99.2	59.79
Ga	18.8	17.2	24.6	22.6	18.8	15.9	25.1	25.5	24.8	24.7	14.6	19.1	17.44
Ge	2.08	2.03	2.48	2.22	1.89	1.54	2.06	1.94	1.85	1.94	0.87	1.73	1.40
Rb	220	212	172	167	293	256	215	204	192	202	112	267	181
Sr	168	163	249	245	153	404	304	322	321	329	128	299	210
Y	28.7	28.3	42.5	40.1	18.8	24.3	36.2	32.4	33.2	31.9	8.31	21.5	14.95
Zr	230	211	227	183	214	235	239	191	171	200	138	251	176
Nb	22.6	24.7	46.3	43.3	16.9	17.5	29.9	28.9	30.5	29.4	11.7	31.3	17.6
Mo	3.47	1.88	10.90	15.60	0.20	0.40	1.50	1.90	2.00	1.40	1.55	921	112
Cs	9.99	7.66	9.94	8.24	9.82	5.90	12.3	12.9	12.5	13.5	5.01	13.8	7.76
Ba	652	681	382	429	419	971	247	213	204	210	302	919	593
La	27.00	29.90	29.40	30.40	35.3	44.4	62.3	56.9	57.4	57.8	19.3	39.8	31.5
Ce	71.50	79.10	90.30	97.20	59.6	86.2	124	113	115	114	41.3	81.6	64.5
Pr	8.53	9.37	11.4	12.2	7.31	10.4	13.6	12.5	13	12.7	4.48	7.99	6.39
Nd	35.30	38.70	45.40	48.20	28.4	41.8	49.3	45.4	47.5	46.2	16.5	27.4	22.19
Sm	8.46	8.40	10.40	10.50	5.79	8.73	9.56	8.94	9.34	8.87	3.50	5.53	4.32
Eu	1.65	1.93	1.74	2.02	1.10	2.05	2.08	1.87	1.92	1.82	0.69	1.20	0.88
Gd	7.57	7.60	9.69	9.74	5.25	8.30	9.31	8.65	8.73	8.43	2.76	4.84	3.95
Tb	1.13	1.09	1.49	1.41	0.70	1.09	1.31	1.16	1.25	1.17	0.34	0.69	0.55
Dy	5.95	5.31	7.87	7.37	3.58	5.19	6.86	6.14	6.28	5.99	1.69	3.83	2.81
Ho	1.20	1.07	1.63	1.53	0.72	0.93	1.37	1.20	1.26	1.20	0.32	0.79	0.56
Er	2.98	2.84	4.20	4.17	1.91	2.30	3.53	3.09	3.25	3.03	0.83	2.03	1.46
Tm	0.42	0.40	0.61	0.58	0.25	0.29	0.48	0.42	0.44	0.41	0.13	0.29	0.21
Yb	2.70	2.61	4.18	4.01	1.83	1.81	3.26	2.85	2.83	2.85	0.84	1.94	1.38
Lu	0.42	0.39	0.63	0.61	0.29	0.25	0.50	0.44	0.43	0.41	0.14	0.29	0.21
Hf	6.71	6.34	7.08	5.74	5.9	5.92	6.19	4.78	4.39	5.34	4.01	7.02	5.19
Ta	1.55	2.46	4.56	4.74	0.82	1.23	2.41	2.42	2.57	2.45	1.60	3.01	2.28
Pb	28.5	29.6	23.8	25.4	40.8	40.9	30.9	26.4	26.5	26.4	18.6	32.5	26.86
Th	17.10	21.30	12.70	19.80	14.2	16.7	12.5	13.8	15.3	12.7	14.1	32.4	22.37
U	6.60	6.28	10.00	10.70	2.89	4.31	4.62	4.39	4.52	4.17	4.88	24.3	10.1
Nb/Ta	14.58	10.04	10.15	9.14	20.61	14.23	12.41	11.94	11.87	12.00	7.31	10.40	7.71
Ce/Pb	2.51	2.67	3.79	3.83	1.46	2.11	4.01	4.28	4.34	4.32	2.22	2.51	2.40
$(La/Yb)_N$	7.17	8.22	5.05	5.44	13.03	16.58	12.91	13.49	13.71	13.7	7.25	26.72	17.38
$(Gd/Yb)_N$	2.32	2.41	1.92	2.01	2.32	3.72	2.32	2.46	2.5	2.4	1.81	3.04	2.44
Eu/Eu*	0.63	0.74	0.53	0.61	0.61	0.74	0.67	0.65	0.65	0.64	0.52	0.75	0.66
Data source	This study										Zhu et al. (2011)		

analyses were performed on a MAT251EM mass spectrometer at the Open Laboratory of Isotope Geochemistry, Ministry of Land and Mineral Resources of China, Wuhan, using methods of Robinson and Kusakabe (1975). Samples were combusted with CuO in an oven at 1000 °C under vacuum. Liberated SO_2 was frozen in a liquid nitrogen trap and after cryogenic separation from other gases. Sulfur isotope ratios are reported as $\delta^{34}S$ relative to the Canyon Diablo Troilite (CDT), with the analytical reproducibility of ±0.2‰.

5.5. Lead isotopes

Lead isotopic compositions of sulfides and K-feldspar from the granite were analyzed at the State Key Laboratory of Continental Dynamics, Northwest University, Xi'an, China. The analytical method was similar to that described by Elburg et al. (2005). The lead isotopes were measured by Nu Plasma HR MC-ICPMS in static mode. Samples were firstly digested with concentrated hydrochloric and hydrofluoric acid in sequence. Lead was separated from its matrix using 0.15 ml quartz ion-exchange columns filled with AG1 × 8, 200 to 400 mesh (Bio-Rad, USA). ICP-MS analyses showed that a single pass through the columns was sufficient to remove all matrix. Lead isotope ratios were determined by adding NBS 997 TI into the samples, and corrected for instrument mass fractionation using $^{205}Tl/^{203}Tl = 2.3872$. Meanwhile, the NBS 981 was used for external correction. The measured isotopic compositions (2σ) of NBS 981 are $^{206}Pb/^{204}Pb = 16.955 \pm 0.001$, $^{207}Pb/^{204}Pb = 15.503 \pm 0.001$, and $^{208}Pb/^{204}Pb = 36.743 \pm 0.002$, while those of BCR-2 are $^{206}Pb/^{204}Pb = 18.750 \pm 0.000$, $^{207}Pb/^{204}Pb = 15.625 \pm 0.000$, and $^{208}Pb/^{204}Pb = 38.712 \pm 0.001$, respectively. The total procedural blank for Pb is between 0.1 and 0.3 ng and the sample to blank ratio is larger than 1800.

6. Results

6.1. Major, trace and rare earth elements (REEs) for host granite and MMEs

The major and trace element compositions of the host granite (summarized from our earlier paper, Zhu et al., 2011) and MMEs from the Wenquan pluton are provided in Table 1. The ten MME samples belong to the metaluminous series and plot within the monzodiorite to monzonite fields (SiO_2 = 52.86–60.51 wt.%; $K_2O + Na_2O$ = 6.76–8.94 wt.%), which is different to the granite (Fig. 6a, b). In comparison to the granite, the MMEs have higher TiO_2 (0.56–1.20 wt.%), CaO (4.47–6.13 wt.%), MgO (4.06–7.18 wt.%) and Mg# (56.5–75.1) contents, similar Al_2O_3 contents (12.59–16.80 wt.%) and lower A/CNK ratios (0.65–0.80). In plots of oxide and trace element ratios versus MgO and SiO_2 (Fig. 7), the granite and MMEs define two distinct regions and trends without any converging linear trend.

Chondrite-normalized REE distribution patterns for the MMEs samples are right inclined ($(La/Yb)_N$ = 5.05–16.58) with enriched LREE and flat HREE patterns ($(Gd/Yb)_N$ = 1.81–3.04) (Fig. 8b), which are similar with those of the granite (Fig. 8a). The primitive mantle-normalized trace element diagrams show that the MMEs have a relative enrichment of Rb, Th, U, Pb, and K and depletion of Ba, Nb, Ta, Sr and Ti (Fig. 8d), which are also similar with those of the granite (Fig. 8c). The MMEs have negative Eu anomalies with Eu/Eu* of 0.52–0.75 which are also close to those of the granite. The minor difference is that the MMEs have Nb/Ta ratios of 9.14 to 20.61 which are higher than 7.31 to 10.40 for the granite.

6.2. LA-ICP-MS zircon U–Pb age of host granite and MMEs

Zircon CL images and U–Pb dating results for the host granite and MMEs are presented in Fig. 9, and Supplementary Table S1. Most zircons are colorless, transparent and euhedral with columnar crystal forms ranging from 100 to 500 μm. In CL images, most zircons exhibit clear oscillatory zoning, which is a typical texture for magmatic zircon (Hanchar and Hoskin, 2003).

Analyses for zircon U–Pb age were performed on samples W3-1 and W9-1 for the granite, and samples W23-1 and HGL-2 for the MMEs (Supplementary Table S1; Fig. 9). With common lead correction, the $^{207}Pb/^{206}Pb$ system is suitable for zircons >1 Ga, while the $^{206}Pb/^{238}U$ system is better suited for zircons <1 Ga (Andersen, 2002). Using ISOPLOT (V.3.02) we have plotted the concordia diagrams and calculated the $^{206}Pb/^{238}U$ weighted average ages (Ludwig, 2003). Zircons from samples W3-1 and W9-1 yielded weighted average $^{206}Pb/^{238}U$ ages of 218 ± 2.4 Ma (2σ, MSWD = 3.0, n = 20) and 221 ± 1.3 Ma (2σ, MSWD = 0.88, n = 19), respectively. These ages are consistent with our previous zircon U–Pb ages of 216 ± 1.7 and 217 ± 2.0 Ma for the granite (Zhu et al., 2011). This grouping of ages is interpreted as the crystallization age of the granite.

Zircons from the MMEs (samples W23-1 and HGL-2) yielded weighted average $^{206}Pb/^{238}U$ ages of 217 ± 2.0 Ma (2σ, MSWD = 2.1, n = 20) and 218 ± 2.5 Ma (2σ, MSWD = 0.43, n = 22), respectively (Fig. 9). These consistent zircon U–Pb ages for the granite and MMEs suggest that the mafic and felsic magmas intruded coevally.

6.3. Zircon Hf isotopic compositions

The results of in situ zircon Lu–Hf isotopic compositions and the corresponding calculated parameters for the granite and the MMEs of the Wenquan pluton are listed in Supplementary Table S2. All of the zircon samples from the granite and MMEs have $^{176}Lu/^{177}Hf$ ratios ranging from 0.000545 to 0.004575, suggesting that these zircons have very low contents of radiogenic Hf accumulation after their formation, so the measured $^{176}Hf/^{177}Hf$ ratios are interpreted to represent the Hf isotopic compositions during formation (Kinny and Maas, 2003).

Sample W3-1 from the granite has $^{176}Hf/^{177}Hf$ ratios of 0.282607 to 0.282646 with a weighted average ratio of 0.282624 ± 0.000011 (2σ, MSMD = 0.47) (Fig. 10) and calculated $\varepsilon_{Hf(t)}$ values ranging from −1.4 to 0.2. Two-stage Hf model ages (T_{DM2}) range from 1112 to 1040 Ma.

Sample W9-1 from the granite has limited $^{176}Hf/^{177}Hf$ variation ranging from 0.282537 to 0.282729 with a weighted average ratio of 0.282604 ± 0.000018 (2σ, MSWD = 7.8) (Fig. 10), which is consistent with sample W3-1. This sample has $\varepsilon_{Hf(t)}$ values ranging from −3.6 to 3.0 with corresponding T_{DM2} of 1234 to 890 Ma.

Samples W23-1 and HGL-2 from MMEs display relatively broader variations in Hf isotopic composition (Fig. 10). Four out of twenty analyzed spots from sample W23-1 returned positive $\varepsilon_{Hf(t)}$ values varying between 0.5 and 10.8 with single-stage Hf model ages (T_{DM1}) between 846 and 441 Ma, while the remaining sixteen analyses returned negative $\varepsilon_{Hf(t)}$ values ranging from −3.2 to −0.2 with T_{DM2} of 1217 to 1065 Ma. For sample HGL-2, three out of twenty two analyzed spots have positive $\varepsilon_{Hf(t)}$ values ranging from 0.0 to 1.9 with T_{DM1} of 865 to 789 Ma, and the remaining nineteen spots returned negative $\varepsilon_{Hf(t)}$ values ranging from −10.1 to −0.1 with T_{DM2} of 1565 to 1052 Ma.

6.4. Molybdenite Re–Os isotopic dating

Re–Os data of the five molybdenite samples are listed in Table 2. Re–Os isochron ages were calculated using ISOPLOT 3.0 (Ludwig, 2003). As molybdenite contains high Re/Os ratios the Re–Os chronometer can be applied to date molybdenum mineralization. Initially molybdenite does not contain common Os, thus all the measured Os is monoisotopic (^{187}Os), the daughter product of ^{187}Re decay (Raith and Stein, 2000). Therefore, the model age is calculated as the following equation:

$$t = \frac{1}{\lambda}\left[\ln\left(1 + \frac{^{187}Os}{^{187}Re}\right)\right]$$

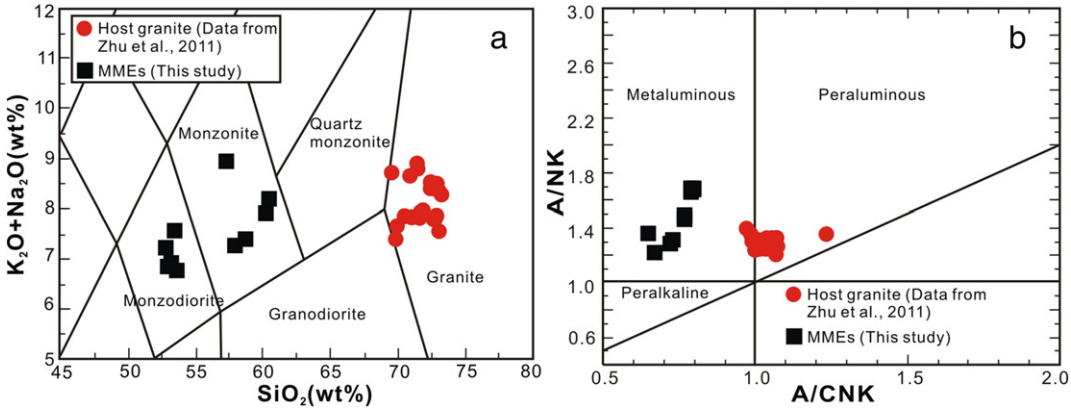

Fig. 6. The total alkali vs. SiO_2 (a) (Middlemost, 1994) and A/CNK vs. A/NK (b) plots of the host granite and MMEs.

where decay constant $\lambda(^{187}Re) = 1.666 \times 10^{-11}a^{-1}$ (Smoliar et al., 1996). The molybdenite samples analyzed contain Re and ^{187}Os values from 3766 to 25206 ppb and 8.54 to 57.42 ppb, respectively. The Re–Os model ages of the five samples are consistent, ranging from 216 ± 2.6 Ma to 220 ± 3.1 Ma, with a weighted mean age of 218 ± 2.3 Ma (Fig. 11b). The isochron age is 219 ± 5.2 Ma (Fig. 11a), with an initial $^{187}Os/^{188}Os$ ratio of −0.076 ± 0.46. The nearly identical model and isochron ages confirm the reliability of the analytical results. Additionally this Re–Os age is similar to the formerly published molybdenite Re–Os isochron age of 214 ± 7.1 Ma for Mo mineralization of the Wenquan deposit (Zhu et al., 2009), and slightly younger than zircon U–Pb ages of the granites and MMEs, indicating that Mo mineralization happened in the late stage of the magmatic activity in late Triassic.

6.5. Lead and sulfur isotopes

Tables 3 and 4 show previously published (Zhu et al., 2011) and new lead and sulfur isotope data for the Wenquan Mo deposit. K-feldspar separated from the granite exhibit limited Pb isotopic compositional variety with $^{206}Pb/^{204}Pb$ ratios of 18.061 to 18.323, $^{207}Pb/^{204}Pb$ ratios of 15.485 to 15.587 and $^{208}Pb/^{204}Pb$ ratios of 37.957 to 38.402. Molybdenite and pyrite exhibit scattered Pb isotopic variability with $^{206}Pb/^{204}Pb$ ratios of

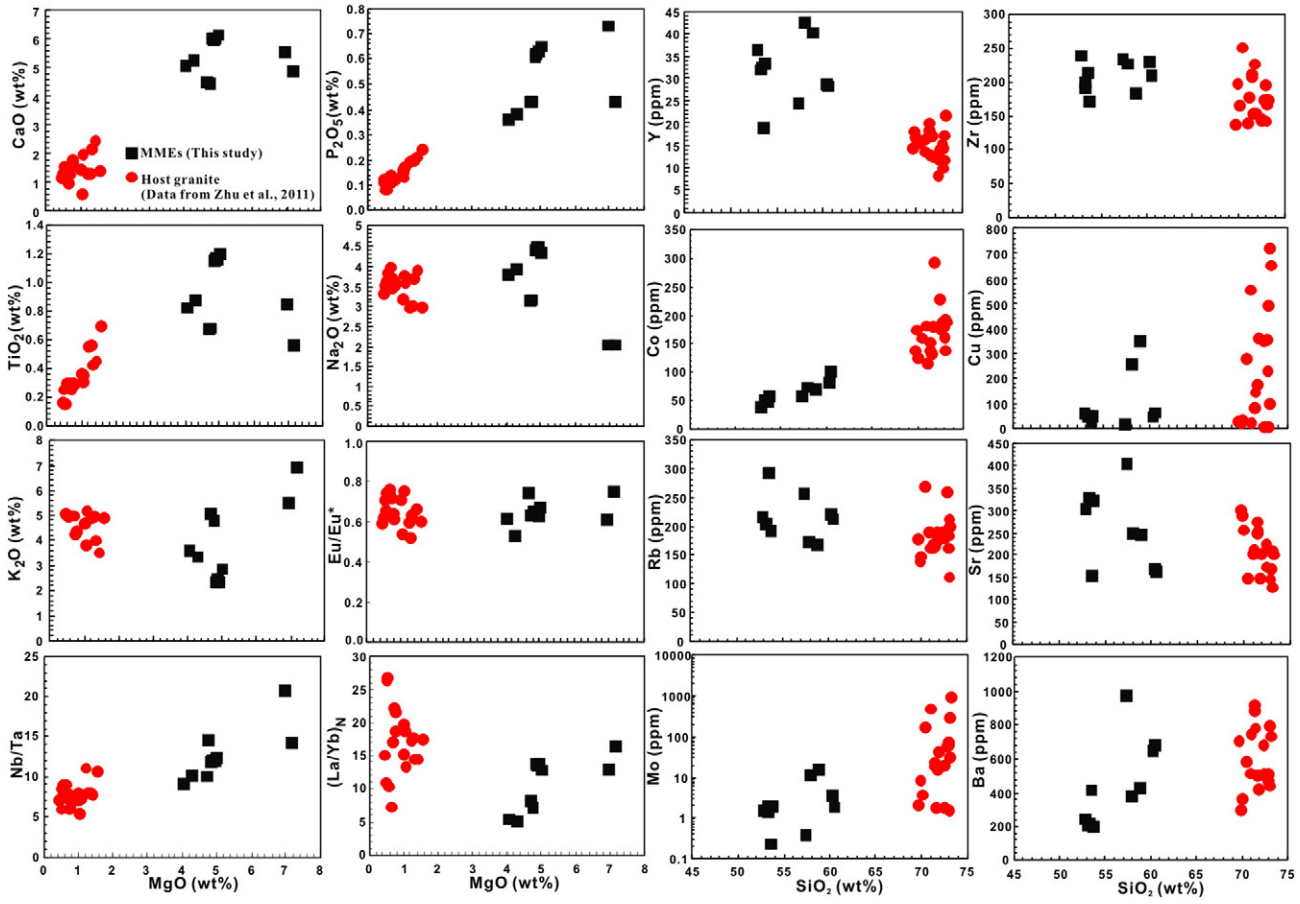

Fig. 7. Various oxide and trace element ratios vs. MgO and SiO_2 diagrams for the host granite and MMEs from the Wenquan pluton.

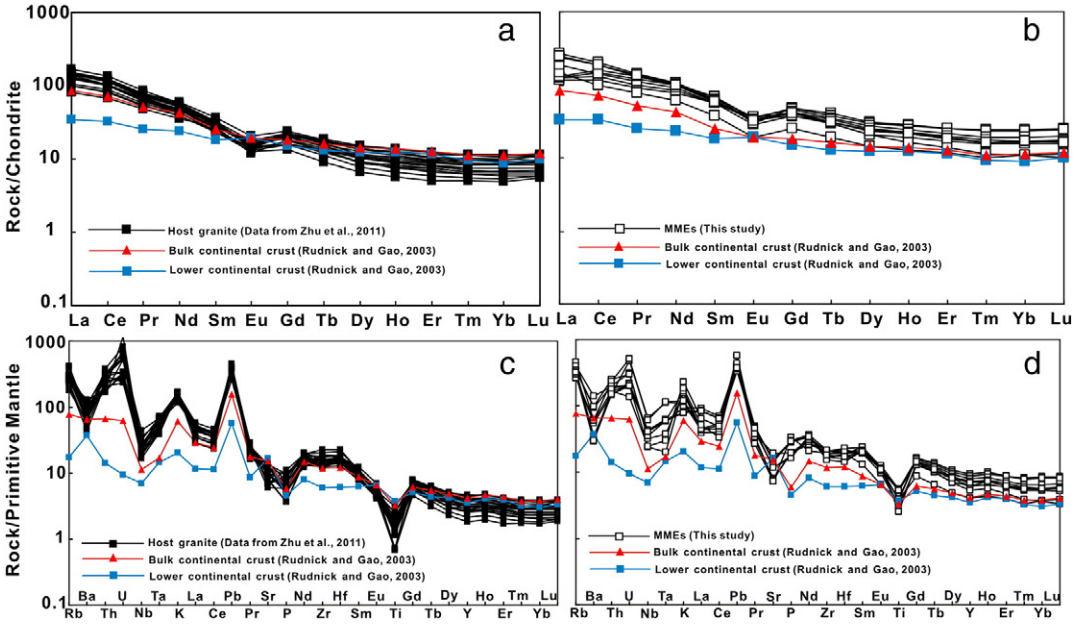

Fig. 8. Chondrite-normalized REE and primitive mantle-normalized (Sun and McDonough, 1989) trace element patterns for the Wenquan granite (a, c) and MMEs (b, d).

17.973 to 19.853, $^{207}Pb/^{204}Pb$ ratios of 15.546 to 15.729 and $^{208}Pb/^{204}Pb$ ratios of 37.973 to 39.349.

The $\delta^{34}S_{CDT}$ values vary from 5.0 to 11.7‰, with a pronounced mode varying in a narrow range between 5.0 and 6.1‰ for 15 samples, and 7.5 to 11.7‰ for the remaining five samples (Fig. 12).

7. Discussion

7.1. Age of Mo mineralization and source of ore-forming materials

The mineralization of the Wenquan Mo deposit is spatially related to magmatic activities. Field observations show that all the Mo mineralization occurs within the granitic pluton and Mo-bearing veins infill or replace primary joints and cracks in the granites (Figs. 4a and 5a), suggesting that the Mo mineralization was mainly generated during the late aqueous and volatile rich phases of magma crystallization. On the other hand, the mineralization of the Wenquan Mo deposit is temporally related to the magmatic activities. The molybdenite Re–Os isochron age of 219 ± 5.2 Ma can be interpreted as the age of Mo mineralization for the Wenquan Mo deposit (Fig. 11) which is statistically indistinguishable with magma crystallization ages of the granite and MMEs determined by the zircon U–Pb dating. This suggests that Mo mineralization and magma mixing processes occurred contemporaneously in the Late Triassic, and that hybrid magma may have played an essential role in generating the Wenquan Mo deposit.

The Pb isotope compositions of K-feldspar in the granite are homogeneous and in good agreement with those of granitoids formed in the SCB (Fig. 13), indicating that the Wenquan granitic magma was derived from middle-lower crust of the SCB. This is also supported by the studies of Zhang et al. (2006, 2007). In the Pb isotopic composition plot (Zartman and Doe, 1981) (Fig. 13), most samples of the Wenquan granite plot near the orogenic Pb evolution line or within the area between the orogenic and mantle Pb evolution lines. This reflects mixing of orogen- and mantle-derived materials. The values of ores are generally variable, but most samples fall in the region near the Wenquan granite and those of the SCB granitoids, reflecting that Pb in ores and granites was derived from the same source. A few samples have higher Pb isotopic ratios than the granite and those of the SCB granitoids, indicating the involvement of upper crustal material in the ore-forming system. As illustrated in Fig. 1, the main strata around the Wenquan Mo deposit are Devonian in age, and therefore the higher Pb isotopic ratios for ores may be related to the addition of radiogenic Pb decayed from U and Th of Devonian sedimentary rocks into the ore-forming fluids. The $\Delta\gamma$ and $\Delta\beta$ values can help establish the lead sources following the equations: $\Delta\gamma = (\gamma - \gamma_M) \times 1000/\gamma_M$ and $\Delta\beta = (\beta - \beta_M) \times 1000/\beta_M$ (γ: $^{208}Pb/^{204}Pb$ of sample; γ_M: $^{208}Pb/^{204}Pb$ of mantle = 37.47; β: $^{207}b/^{204}Pb$ of sample; β_M: $^{207}b/^{204}Pb$ of mantle = 15.33; after Zhu, 1998). In the $\Delta\gamma$–$\Delta\beta$ diagram (Fig. 14), most K-feldspar and sulfide samples overlap the fields of mixed upper crust and mantle lead caused by magmatism, which further suggests that the Wenquan pluton was a possible source for the ore-forming materials. Combined above the field observations (Figs. 4a and 5a) with the $\Delta\gamma$ and $\Delta\beta$ calculations, it can be argued that rather than a major Pb contribution from sedimentary rocks, Pb composition mainly originated from granitic melts and mixed with the Pb in ore-forming solution derived from the fractional crystallization of a Triassic magmatic fluid evolution system. Considering the above, we propose that the ore-forming materials and the Wenquan granites were mainly derived from a hybrid magma of lower crust and mantle, and the Mo mineralization was generated during the late aqueous and volatile-rich phase of magma crystallization in the Late Triassic.

The $\delta^{34}S$ values of total S (i.e. $\sum S$) in the fluids can be used as an indicator of their source (Ohmoto, 1972). In hydrothermal systems, where H_2S is the dominant sulfur species in the fluids or the fluid redox state is below the SO_2/H_2S boundary, a relation exists as $\delta^{34}S_{sulfide} \approx \delta^{34}S_{H_2S} \approx \delta^{34}S_{fluid}$ (Kelly and Rye, 1979; Rollinson, 1993). So the average $\delta^{34}S$ values of sulfide minerals approximate the $\delta^{34}S$ values of hydrothermal fluids. In the Wenquan deposit pyrite and molybdenite are the main sulfides in the ore-bearing veins. The lack of oxide phases, sulfate minerals or chloritization in the ores suggests that H_2S might be the dominant sulfur species and thus the average $\delta^{34}S$ values of sulfides can be considered to directly represent the $\delta^{34}S$ values of the hydrothermal fluids. Sulfides from the Wenquan Mo deposit have two groups of $\delta^{34}S$, implying at least two sources. But most $\delta^{34}S$ values cluster between 5.0 and 6.1‰ (averaging at 5.5‰) (Table 4; Fig. 12) and these relatively homogeneous $\delta^{34}S$ values of the Wenquan deposit are close to the $\delta^{34}S$ values of the fluid (~5.0‰) in equilibrium with granite magma ($\delta^{34}S$ = 0.0‰) (Ohmoto, 1972), implying a magmatic control in mineralization. The $\delta^{34}S_{CDT}$ values of ores from the Wenquan deposit are higher than that of mantle-derived sulfur, but fall within the range of porphyry Mo and Climax-type Mo deposits (0.8‰ to 6.8‰) (Carten et al., 1993), and similar to

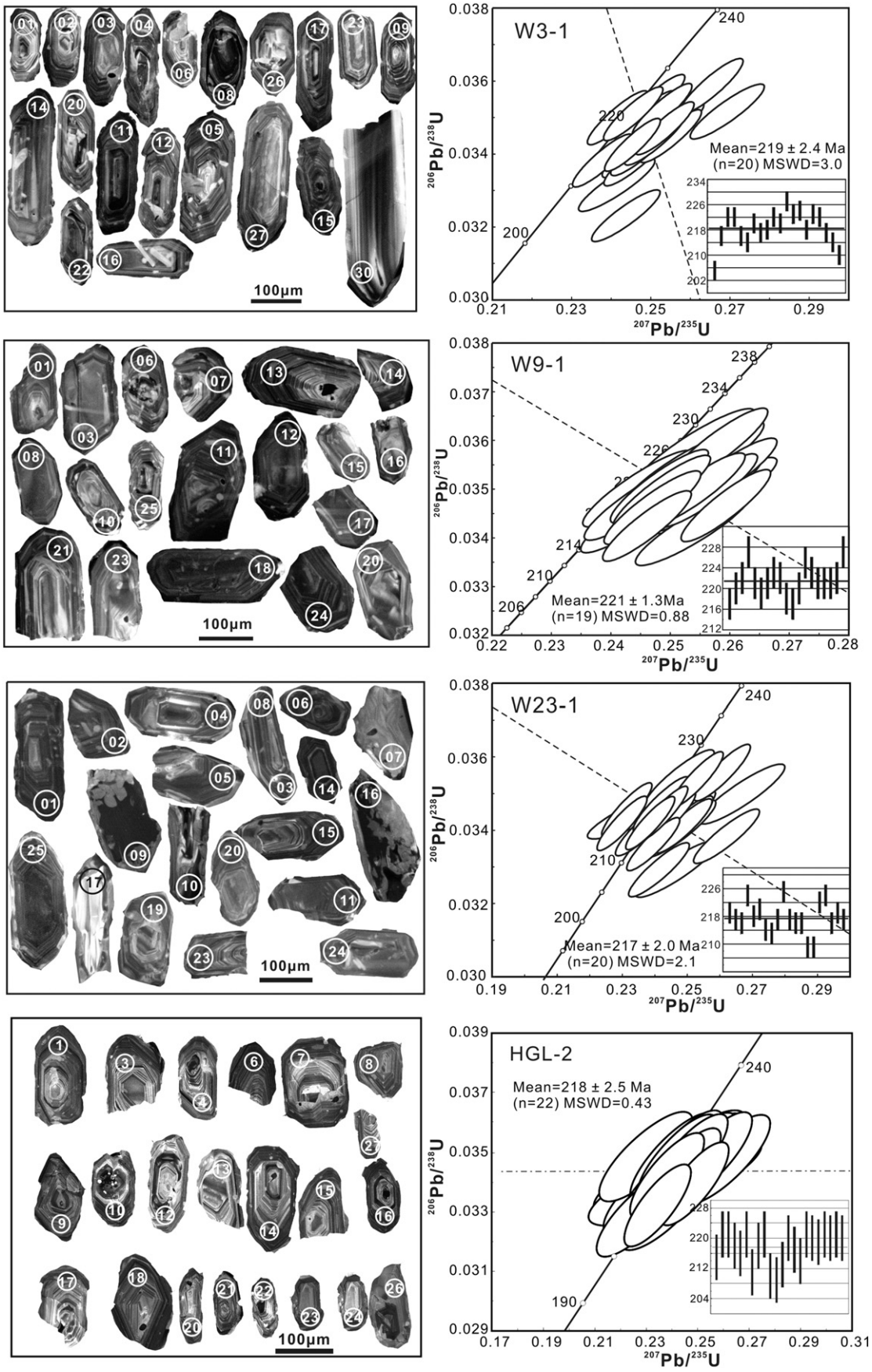

Fig. 9. CL images and LA-ICP-MS U–Pb zircon concordia diagrams of the host granite (W3-1 and W9-1) and MMEs (W23-1 and HGL-2). Ellipse dimensions are 2σ.

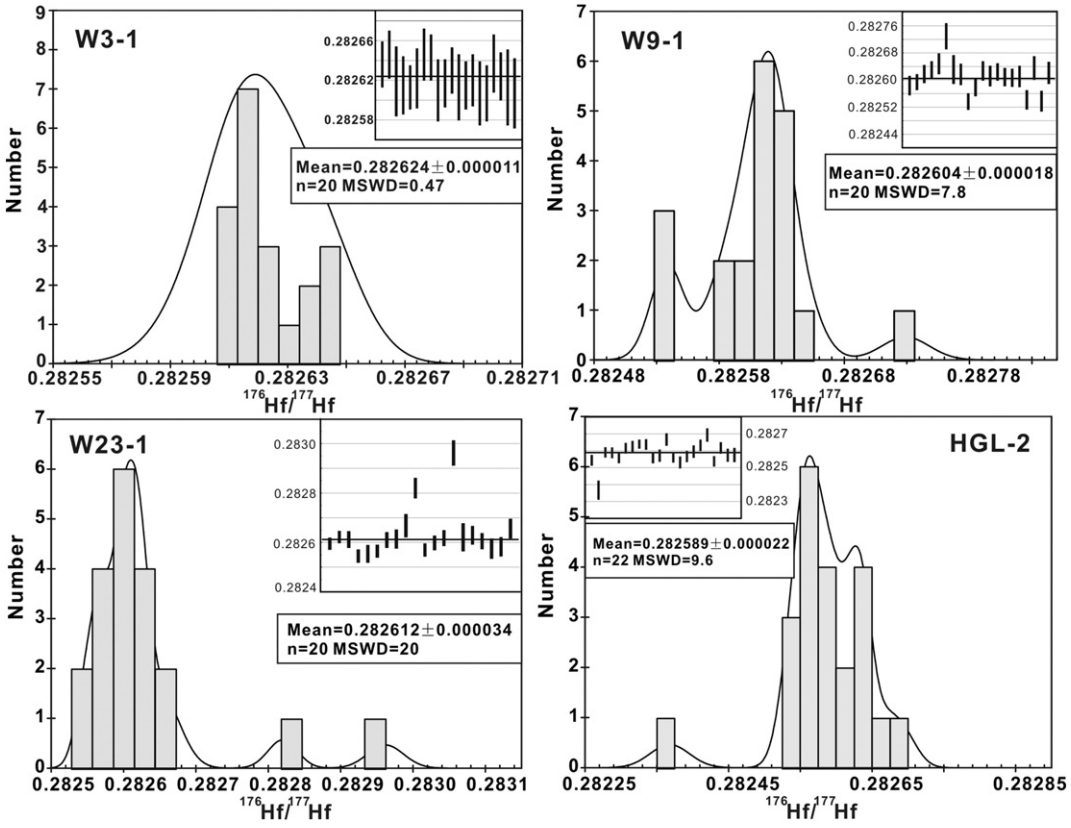

Fig. 10. Histograms of zircon $^{176}Hf/^{177}Hf$ ratios for the host granite and MMEs.

those of typical magmatic–hydrothermal systems (Ohmoto, 1972). Although a few samples contain high $\delta^{34}S$ values from 7.5 to 11.7‰, which would imply a shallow source for some of the sulfur (20‰, Rollinson, 1993). Hence we suggest that the sulfur of the Wenquan Mo deposit mainly originated from magmatic–hydrothermal fluid associated with the granitic pluton and subordinately from the contamination of heavy sulfur from strata. Moreover, previous studies by Wang et al. (2012) showed that the $\delta^{13}C_{PDB}$ values range from −8.3‰ to −7.9‰ for calcite from calcite–quartz veins, which are within the limit of a typical magmatic source (−4‰ to −8‰, Ohmoto, 1972), although these values are also coincident with atmospheric CO_2 (−8‰, Schidlowski, 1998). The calculated $\delta^{18}O_{H_2O}$ values of −0.9 to 0.6‰ for quartz from ore-bearing quartz veins (Ren, 2009) are typical of cycling meteoric water, which could be well interpreted as an influx and mixing of meteoric water with magmatic hydrothermal fluids in the late stages of the mineralization (Chen et al., 2009).

Re–Os isotopes can be used to trace ore-forming material and to estimate the contribution degree of different materials from various sources (Foster et al., 1996). Mao et al. (1999) suggested to take Re content as an index for judging the metallogenic sources of metal sulfide deposits. Based on studies of the molybdenite Re–Os isotopic compositions for intermediate-acid rocks-related Mo deposits in China, it is found that the Re content in ore-forming materials derived from a mixed crust–mantle source can reach tens μg/g (Mao et al., 1999; Li et al., 2007; Meng et al., 2007; Zhu et al., 2008), while in the deposits with a crustal source the Re content in molybdenite can lower to a value of ≤1 − n μg/g. The molybdenite samples from the Wenquan deposit have the Re content of 17 to 25 μg/g (Table 2), indicating a mixed crust–mantle source for the ore-forming materials.

7.2. Magma mixing and genesis of MMEs

The genesis of porphyry Cu–Mo–Au deposits have been thought to be in a close relation with the highly oxidized magmatic systems having high water and sulfur contents (Mungall, 2002; Richards, 2011; Ma et al., 2013). Experimental studies have demonstrated that felsic melts usually have low metal and sulfur solubility (Hattori and Keith, 2001; Mungall, 2002) and that the lower crust is depleted in metals (Cameron, 1989). As a result, chalcophile and siderophile elements are dominated by mantle sulfides (Hamlyn et al., 1985; Sillitoe, 1997). Moreover, intermediate-acidic melts derived from the mafic lower crust have limited water content (Petford and Gallagher, 2001), but

Table 2
Molybdenite Re–Os isotope analytical results of the Wenquan Mo deposit.

Sample no.	Sample weight (g)	Re (ng/g) ± 1σ	Common Os (ng/g) ± 1σ	Re^{187} (ng/g) ± 1σ	Os^{187} (ng/g) ± 1σ	Model age (Ma) ± 1σ
WQ14-M8	0.0182	16880 ± 226	0.23 ± 0.01	10567 ± 141	38.06 ± 0.46	216 ± 2.6
WQ14-M9	0.0205	18896 ± 126	0.26 ± 0.001	11829 ± 79	43.32 ± 0.57	219 ± 2.9
WQ14-M13	0.0234	3766 ± 15	0.17 ± 0.02	2358 ± 9	8.54 ± 0.17	217 ± 4.3
W-21	0.0173	25206 ± 489	0.24 ± 0.03	15779 ± 306	57.42 ± 0.51	218 ± 1.9
W24-2	0.0194	18154 ± 241	0.21 ± 0.01	11364 ± 151	41.66 ± 0.59	220 ± 3.1
GBW04436 (JDC)	0.0144	17577 ± 177	0.32 ± 0.01	11003 ± 111	25.48 ± 0.48	139 ± 2.6
GBW04436 (JDC)	0.0144	17228 ± 140	0.52 ± 0.02	10785 ± 87	24.88 ± 0.37	138 ± 2.1

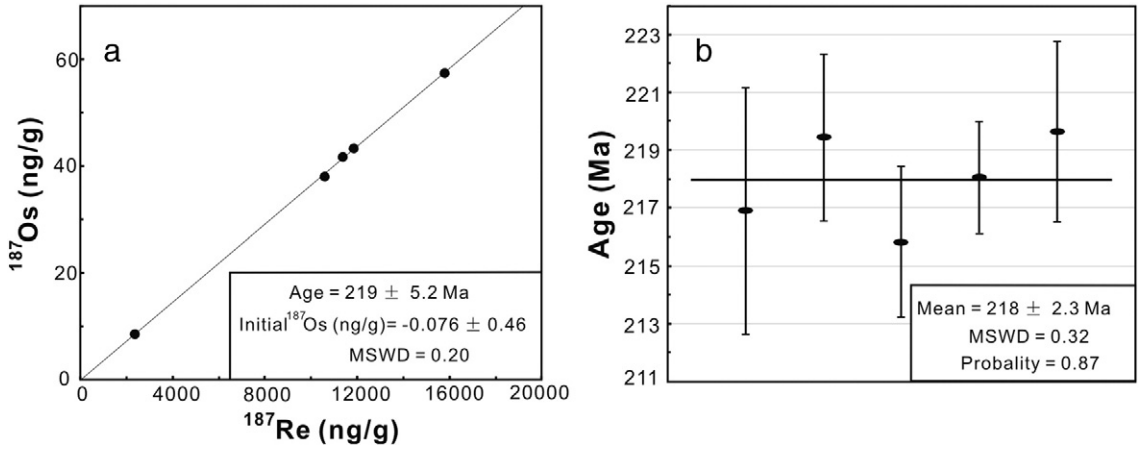

Fig. 11. Re–Os isochron age (a) and weighted average of model ages (b) of the Wenquan Mo deposit.

the involvement of mafic magma derived from the mantle could not only compensate the water for the intermediate-acid melts, but also change their fO_2 (Chiaradia et al., 2012). With the dropping of temperature and pressure, hydrous magmas can release a water-rich volatile phase to form a magmatic–hydrothermal ore-forming system (Burnham, 1997), where the sulfur and metals are transferred directly from mafic to felsic melts as a result of magma mixing (Keith et al., 1997; Hattori and Keith, 2001; Halter et al., 2002; Audetat and Pettke, 2006; Stern et al., 2007).

The essential role of mantle-derived materials in the formation of porphyry-related Mo–Cu deposits has been widely accepted, although the exact mechanism remains disputed (Keith et al., 1997; Maughan et al., 2002; Ma and chen, 2011; Ma et al., 2013). The widespread existence of MMEs in granitoids is often cited as the strong evidence for injection of mafic magma from mantle sources (discussed below). Besides the Wenquan porphyry Mo deposit, the MMEs have been seen in numerous porphyry deposits globally, such as the Farallón Negro porphyry in Argentina (Halter et al., 2004), the Aolunhua porphyry in Inner Mongolia (Ma et al., 2013), the Pulang (Cao et al., 2009) and Machangqing (Guo et al., 2012) porphyries in Yunnan, the Tongguanshan porphyry in Anhui (Y.S. Du et al., 2004) and the Qulong porphyry in Tibet (Yang et al., 2008). Although the MMEs in porphyry-related Mo–Cu deposits are common, the consensus on their mechanism have not been reached, which promotes us to study the MMEs in the Wenquan Mo deposit.

The linear chemical variation as a major feature for the restite unmixing model can be observed in many plutonic suites (Chappell et al., 1987; Chappell and White, 1992; Collins, 1998). However, the feature cannot be seen in most element variation diagrams for the Wenquan pluton (Fig. 7). As illustrated in Fig. 7, when MgO and SiO_2

Table 3
Lead isotope data of sulfides and K-feldspar from the Wenquan Mo deposit.

Sample no.	Sample description	$^{206}Pb/^{204}Pb$	$^{207}Pb/^{204}Pb$	$^{208}Pb/^{204}Pb$	Δγ	Δβ	Source
W1-2	K-feldspar in porphyritic monzogranite	18.32277 ± 0.00056	15.56284 ± 0.00045	38.40229 ± 0.00133	24.9	15.2	This study
W16-2	K-feldspar in biotite monzogranite	18.06088 ± 0.00047	15.56484 ± 0.00057	38.24573 ± 0.00200	20.7	15.3	This study
W28-4	K-feldspar in biotite monzogranite	18.06349 ± 0.00054	15.55969 ± 0.00042	38.19233 ± 0.00106	19.3	15.0	This study
WQ14-G1	K-feldspar in porphyritic monzogranite	18.26861 ± 0.00036	15.58688 ± 0.00032	38.33396 ± 0.00106	23.1	16.8	This study
WQ14-G2	K-feldspar in porphyritic monzogranite	18.13178 ± 0.00031	15.57128 ± 0.00030	38.23742 ± 0.00137	20.5	15.7	This study
WQ14-G3	K-feldspar in pyritization biotite monzogranite	18.09568 ± 0.00037	15.55494 ± 0.00036	38.15248 ± 0.00096	18.2	14.7	This study
WQ14-G4	K-feldspar in pyritization biotite monzogranite	18.25816 ± 0.00037	15.55707 ± 0.00033	38.38974 ± 0.00086	24.5	14.8	This study
WQ14-M5	Film-like molybdenite from molybdenite-bearing quartz vein	18.09688 ± 0.00047	15.56127 ± 0.00038	38.18782 ± 0.00109	19.2	15.1	This study
WQ14-M6	Scaly molybdenite from molybdenite-bearing quartz vein	18.32034 ± 0.00038	15.57914 ± 0.00031	38.30754 ± 0.00087	22.4	16.3	This study
WQ14-M7	Film-like molybdenite from molybdenite-bearing quartz vein	18.49385 ± 0.00070	15.59031 ± 0.00067	38.59740 ± 0.00206	28.9	16.1	This study
WQ14-M8	Film-like molybdenite from molybdenite-bearing quartz vein	19.00880 ± 0.00053	15.61370 ± 0.00040	38.48956 ± 0.00137	27.2	18.5	This study
WQ14-M9	Film-like molybdenite from molybdenite-bearing quartz vein	19.46751 ± 0.00039	15.64132 ± 0.00034	39.34908 ± 0.00102	50.1	20.3	This study
WQ14-M10	Film-like molybdenite from molybdenite-bearing quartz vein	19.28044 ± 0.00051	15.62116 ± 0.00041	38.29770 ± 0.00120	22.1	19.0	This study
WQ14-M11	Molybdenite radiated aggregation from potassic-altered granite	18.32302 ± 0.00049	15.58169 ± 0.00038	38.31265 ± 0.00121	22.5	16.4	This study
WQ14-M13	Disseminated molybdenite from molybdenite–quartz–K-feldspar vein	17.97272 ± 0.00053	15.56811 ± 0.00053	38.13877 ± 0.00147	17.8	15.5	This study
WQ14-G2-1	Disseminated pyrite from molybdenite–pyrite–quartz vein	18.14891 ± 0.00032	15.55507 ± 0.00026	38.28559 ± 0.00088	21.8	14.7	This study
W3-3	K-feldspar in biotite monzogranite	18.067 ± 0.009	15.485 ± 0.007	37.957 ± 0.016	13.0	10.1	Zhu et al. (2011)
W8-2	K-feldspar in biotite monzogranite	18.080 ± 0.003	15.529 ± 0.003	38.098 ± 0.008	16.8	13.0	Zhu et al. (2011)
W9-2	K-feldspar in biotite monzogranite	18.084 ± 0.005	15.577 ± 0.003	38.278 ± 0.015	21.6	16.1	Zhu et al. (2011)
W17-5	K-feldspar in biotite granite	18.077 ± 0.005	15.570 ± 0.004	38.245 ± 0.011	20.7	15.7	Zhu et al. (2011)
W25-4	K-feldspar in porphyritic monzogranite	18.128 ± 0.007	15.564 ± 0.004	38.236 ± 0.019	20.4	15.3	Zhu et al. (2011)
W25-5	K-feldspar in porphyritic monzogranite	18.070 ± 0.001	15.561 ± 0.001	38.142 ± 0.004	17.9	15.1	Zhu et al. (2011)
W9-1	Molybdenite-bearing quartz vein	19.195 ± 0.005	15.605 ± 0.005	38.182 ± 0.016	19.0	17.9	Zhu et al. (2011)
W10-1	Molybdenite-bearing quartz vein	18.047 ± 0.007	15.574 ± 0.005	38.108 ± 0.017	17.0	15.9	Zhu et al. (2011)
W10-2	Molybdenite-bearing quartz vein	17.987 ± 0.003	15.546 ± 0.003	37.973 ± 0.011	13.4	14.1	Zhu et al. (2011)
M-1	Molybdenite from molybdenite-bearing quartz vein	18.197 ± 0.008	15.570 ± 0.007	38.278 ± 0.017	21.6	15.7	Zhu et al. (2011)
W9-1	Molybdenite from molybdenite-bearing quartz vein	18.678 ± 0.004	15.646 ± 0.005	39.039 ± 0.008	41.9	20.6	Zhu et al. (2011)
W18-1	Molybdenite from molybdenite-bearing quartz vein	19.853 ± 0.016	15.729 ± 0.010	39.034 ± 0.012	41.7	26.0	Zhu et al. (2011)
W20-2	Molybdenite from molybdenite-bearing quartz vein	19.646 ± 0.009	15.565 ± 0.007	38.472 ± 0.016	26.7	15.3	Zhu et al. (2011)
W-21	Molybdenite from molybdenite-bearing quartz vein	18.511 ± 0.003	15.582 ± 0.003	38.403 ± 0.006	24.9	16.4	Zhu et al. (2011)
W-24	Molybdenite from molybdenite-bearing quartz vein	19.597 ± 0.008	15.639 ± 0.005	38.408 ± 0.012	25.0	20.2	Zhu et al. (2011)
YX-3	Pyrite from thin molybdenite–pyrite–quartz vein	17.991 ± 0.009	15.631 ± 0.007	38.326 ± 0.015	22.8	19.6	Zhu et al. (2011)

Table 4
Sulfur isotope compositions of sulfides from the Wenquan Mo deposit.

Sample no.	Sample description	$\delta^{34}S_{CDT}$ (‰)	Source
WQ14-M1	Film-like molybdenite from molybdenite–pyrite–quartz vein	11.2	This study
WQ14-M3	Film-like molybdenite from molybdenite-bearing quartz vein	9.0	This study
WQ14-M4	Film-like molybdenite from molybdenite-bearing quartz vein	7.5	This study
WQ14-M5	Film-like molybdenite from molybdenite-bearing quartz vein	11.7	This study
WQ14-M7	Film-like molybdenite from molybdenite-bearing quartz vein	9.6	This study
WQ14-M8	Film-like molybdenite from molybdenite-bearing quartz vein	6.1	This study
WQ14-M10	Film-like molybdenite from molybdenite-bearing quartz vein	5.8	This study
WQ14-M12	Scaly molybdenite from molybdenite–quartz–K-feldspar vein	5.4	This study
WQ14-M13	Disseminated molybdenite from molybdenite–quartz–K-feldspar vein	5.0	This study
WQ14-G2-1	Disseminated pyrite from molybdenite–pyrite–quartz vein	5.4	This study
M-1	Molybdenite from molybdenite-bearing quartz vein	5.5	Zhu et al. (2011)
W9-1	Molybdenite from molybdenite-bearing quartz vein	5.7	Zhu et al. (2011)
W18-1	Molybdenite from molybdenite-bearing quartz vein	5.6	Zhu et al. (2011)
W20-2	Molybdenite from molybdenite-bearing quartz vein	5.5	Zhu et al. (2011)
W-21	Molybdenite from molybdenite-bearing quartz vein	5.6	Zhu et al. (2011)
W-24	Molybdenite from molybdenite-bearing quartz vein	5.6	Zhu et al. (2011)
YX-3	Pyrite from thin molybdenite–pyrite–quartz vein	5.6	Zhu et al. (2011)
YX-6	Pyrite from thin molybdenite–pyrite–quartz vein	5.5	Zhu et al. (2011)
W24-1	Pyrite from thin molybdenite–pyrite–quartz vein	5.0	Zhu et al. (2011)
W20-1	Pyrite from thin molybdenite–pyrite–quartz vein	5.6	Zhu et al. (2011)

are chosen as abscissas for the variation diagrams, the granite and MMEs occupy different regions and unlike the granite, the MMEs do not show any clear trend for most major element and trace element ratios. In the selected oxides, $(La/Yb)_N$, Eu/Eu*, and Nb/Ta ratios versus MgO diagrams (Fig. 7), there are no converging linear trends that incorporate both the enclaves and granite, and the MMEs have lower A/CNK values (0.65–0.80) than those of the granite (0.99–1.06) (Table 1). In the total alkali versus SiO_2 and A/CNK versus A/NK (Fig. 6) diagrams, the clearly plotted differences between the MMEs and granite rule out a cogenetic origin. Furthermore, the MgO versus FeO_{Total} diagram (Fig. 15c) also demonstrates that magma mixing, rather than fractional crystallization, was the dominant mechanism in the generation of the MMEs and granite. Such above geochemical variations are likely interpreted in terms of a two-end-member interaction as the basic process for the genesis of the MMEs and the host rocks.

The magma mixing process is also supported by the following petrographical evidence: (1) The MMEs have rounded to ovoid shapes, with no evidence of solid-state deformation. In most cases, the contacts between the enclaves and host rocks are vague (Fig. 5b, c), reflecting hybridization of mafic and felsic magmas. (2) Some K-feldspar megacrysts occurring in the granite cross-cut the contacts between the host rocks and MMEs, and even enter the MMEs (Fig. 5c), indicating mechanical transfer of mineral grains from a felsic magma into a mafic magma during magma mixing (Vernon et al., 1988). This implies that there was only a small rheological contrast between the two magmas, which had been co-existing for sufficient time allowing crystal transportation from the host felsic magma into the mafic magma (Waight et al., 2000; Perugini et al., 2003; Qin et al., 2009). (3) Abnormal zoning of plagioclase (Fig. 5i) representing a sudden change of crystallization environment is usually cited as an important evidence of magma mixing (Li et al., 2003b; Kemp, 2004; Browne et al., 2006). (4) Lopsided texture types among minerals without support by the normal sequence of crystallization, such as biotite and hornblende containing plagioclase or quartz inclusions (Fig. 5h), reflect that the SiO_2 content decreased dramatically, or the mafic component and plagioclase content increased suddenly (Bateman, 1993). Moreover, feldspar wrapping the biotite, amphibole and feldspar crystallites further indicates that there were at least two mineral generations resulting from the magma mixing (Fig. 5i). (5) Acicular apatite habits are common in mingled mafic pillows (Vernon et al., 1988) and have been attributed to rapid cooling, the result of mingling of small volumes of hot basalt with a cool granitic melt (Sparks and Marshall, 1986). Hence, abundance of acicular apatite in the MMEs further confirms magma mixing as an important process in the formation of the MMEs and their host rocks (Barbarin and Didier, 1992) (Fig. 5g, i). (6) Typical igneous textures and lack of cumulative textures in the MMEs represent a mafic component added to intermediate or felsic magma chambers and argue against the model of minerals cumulating from a mafic magma (Eichelberger, 1980; Vernon, 1984; Vernon et al., 1988; Didier and Barbarin, 1991; Bonin, 2004; Barbarin, 2005; Yang et al., 2006, 2007). (7) Mafic phases are able to nucleate more quickly than felsic phases (Weinberg et al., 2001), so biotite and amphibole proportions in cognate restite of granite origin are greater than 50 vol.% (Rapp and Watson, 1995). However, such a phenomenon of high modal ferromagnesian content has not been observed in our study and thus a cognate origin for the MMEs can be ruled out.

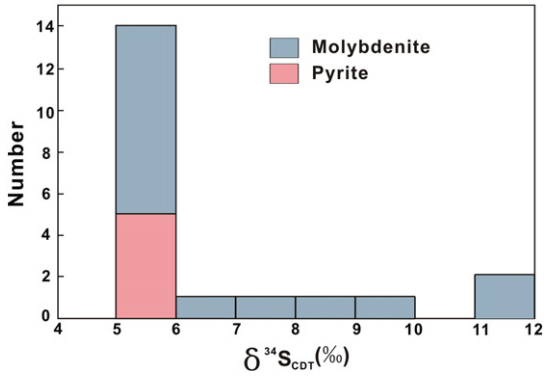

Fig. 12. $\delta^{34}S$ histogram for sulfides from the Wenquan Mo deposit.

The MMEs have relatively low SiO_2 content (52.86–60.51%) and high Mg# (56.5–75.1). According to previous studies, generating intermediate-mafic magma can have two ways: (1) melting of mafic lower crust; and (2) melting of mantle lithosphere. Experimental (Helz, 1976; Rapp et al., 1991; Wolf and Wyllie, 1994) and theoretical studies (Roberts and Clemens, 1993) suggest that dehydrating basaltic lower crust can produce large volumes of mafic melts, particularly in regions with high heat flow that facilitates higher degree partial melting (40%–60%) to form mafic liquids of basaltic and basaltic andesite compositions (Rapp and Watson, 1995). However, these mafic liquids are mostly marked by low MgO and high Al_2O_3, which are not the case of our MMEs. As shown in Fig. 15a, b, the MMEs have Mg#s and K_2O/Na_2O ratios significantly higher than the values of experimental melts of basaltic materials (Sen and Dunn, 1994; Rapp and Watson, 1995) and the high-Mg quartz diorites produced by melting of the mafic lower crust in the Damara Orogen of Namibia (Jung et al., 2002), which indicates that they cannot be produced by partial melting of lower

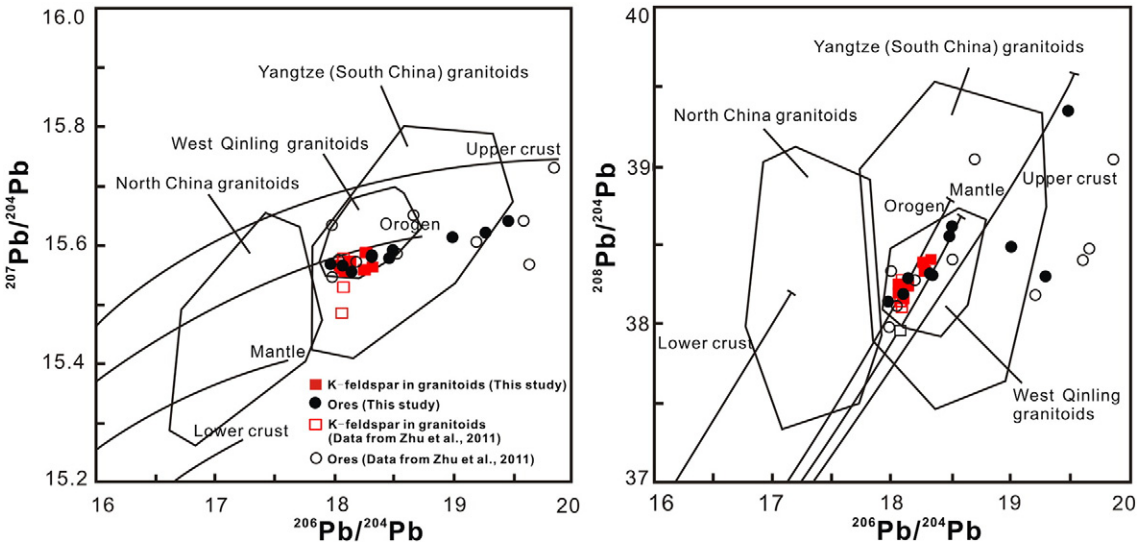

Fig. 13. $^{207}Pb/^{204}Pb$ vs. $^{206}Pb/^{204}Pb$ and $^{208}Pb/^{204}Pb$ vs. $^{206}Pb/^{204}Pb$ diagrams. K-feldspar Pb isotope ratios of Mesozoic granitoids for the North China and Yangtze granitoids are from Zhang (1995). Whole-rock Pb isotope ratios of Indosinian granitoids for the West Qinling are from Zhang et al. (2007). Pb isotopic evolution lines of upper crust, lower crust, orogen and mantle are from Zartman and Doe (1981).

crust. Furthermore, high Nb/Ta (9.14–20.61) ratios indicate that they were most likely derived from a mantle source as partly confirmed by the Ni versus Cr variation diagram (Fig. 15d) (Tsuchiya et al., 2005). The MMEs have lower Ni (8.7–189 ppm) and Cr (66–547 ppm) relative to unfractionated basalt (200–450 ppm and >1000 ppm, respectively, Karsli et al., 2007) suggesting an ultramafic source that underwent fractionation of olivine, pyroxene and spinel prior to interaction with felsic magma. The above criteria demonstrate that partial melting of lithospheric mantle, rather than lower continental crust produced the MMEs.

This view is further verified by the zircon Hf isotope compositions. Zircons in the enclaves have identical U–Pb ages and similar Hf isotopic compositions to those in the granite (Supplementary Tables S1 and S2; Fig. 9), indicating that these zircons were introduced or transferred by magma mingling. Additionally, zircons in the enclaves have a large range of $\varepsilon_{Hf(t)}$ values (−3.2 to 10.8 for sample W23-1; −10.1 to 1.9 for sample HGL-2) (Supplementary Table S2; Fig. 16) that overlap values of the granites and zircons with positive $\varepsilon_{Hf(t)}$ values do exist in both

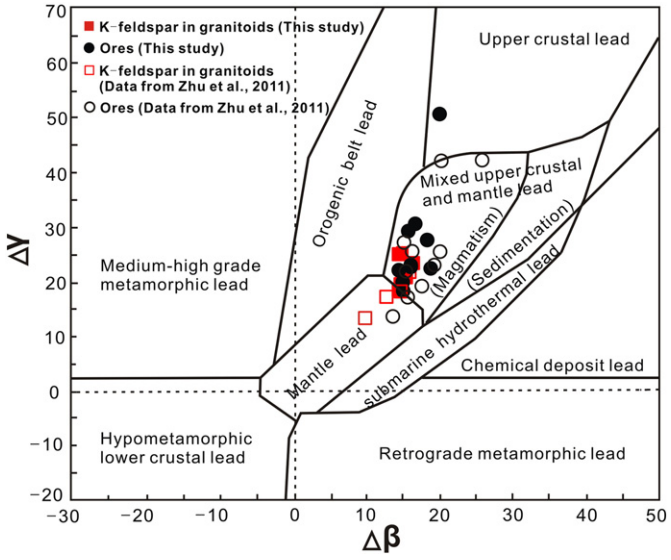

Fig. 14. Δγ vs. Δβ diagram of K-feldspar and ores Pb from the Wenquan Mo deposit. After Zhu (1998).

MMEs and the granite, although the proportion of these zircons is different. The positive $\varepsilon_{Hf(t)}$ values of zircons in the MMEs (Supplementary Table S2) were considerably lower than the Hf isotope ratios of the Triassic depleted mantle (Zheng et al., 2006). Zircons from MMEs (samples W23-1 and HGL-2) not only display a relatively wide variation in Hf isotopic composition (Fig. 10), but also have T_{DM1} of 865 to 441 Ma for the grains with positive $\varepsilon_{Hf(t)}$ values (0.0 to 10.8) and T_{DM2} of 1565 to 1052 Ma for the grains with negative $\varepsilon_{Hf(t)}$ values (−10.1 to −0.1). Since the Hf model ages are much older than the zircon U–Pb ages of the MMEs (217 ± 2.0 Ma and 218 ± 2.5 Ma), the zircons could not have been formed by reworking of the Triassic SCLM (subcontinental lithospheric mantle). Instead, they would have been formed by reworking of the Neoproterozoic SCLM in association with the contemporaneous formation of juvenile crust during rift magmatism along the western and northern margins of the SCB (Zheng et al., 2006, 2007; Zheng, 2008). Hence, zircons in the MMEs with Triassic ages and a heterogeneous distribution of Hf isotopic compositions do not conclude a simple crystallization history, but rather indicate the presence of two discrete magmas: one derived from Neoproterozoic SCLM and the other from pre-existing crustal material were involved in their genesis.

7.3. Genesis of granite

The granite is peraluminous and characterized by high Sr and Ba abundances and highly fractionated REE patterns with negligible Eu anomalies (Table 1; Fig. 8). These characteristics are similar to those of granite originating from ancient crust (Harris et al., 1986; Taylor and McLennan, 1995; Rudnick and Gao, 2003). Most zircons in the granite have negative $\varepsilon_{Hf(t)}$ values and Hf model ages of 1234 to 890 Ma (Supplementary Table S2), indicating that the granite was derived from the Late Mesoproterozoic crust via partial melting. Additionally, the Hf model ages here are similar to the Hf model ages of the Neoproterozoic magmatism in the SCB (Zheng, 2008) including protoliths of UHP metamorphic rocks in the Dabie–Sulu orogenic belt (Zheng et al., 2009). In the $\varepsilon_{Hf(t)}$ versus age plot (Fig. 16), most samples from the granite fall in the area on the evolutionary trend line of the juvenile crust, and are consistent with the magma derived from the reworked Late Mesoproterozoic crust. Therefore, the granite could have been sourced from the Neo-Mesoproterozoic crust of the SCB that was reworked in the subsequent continental collision during Late Triassic.

However, our observation and geochemical data as mentioned above are strongly in favor of mixing of crustal- and mantle-derived

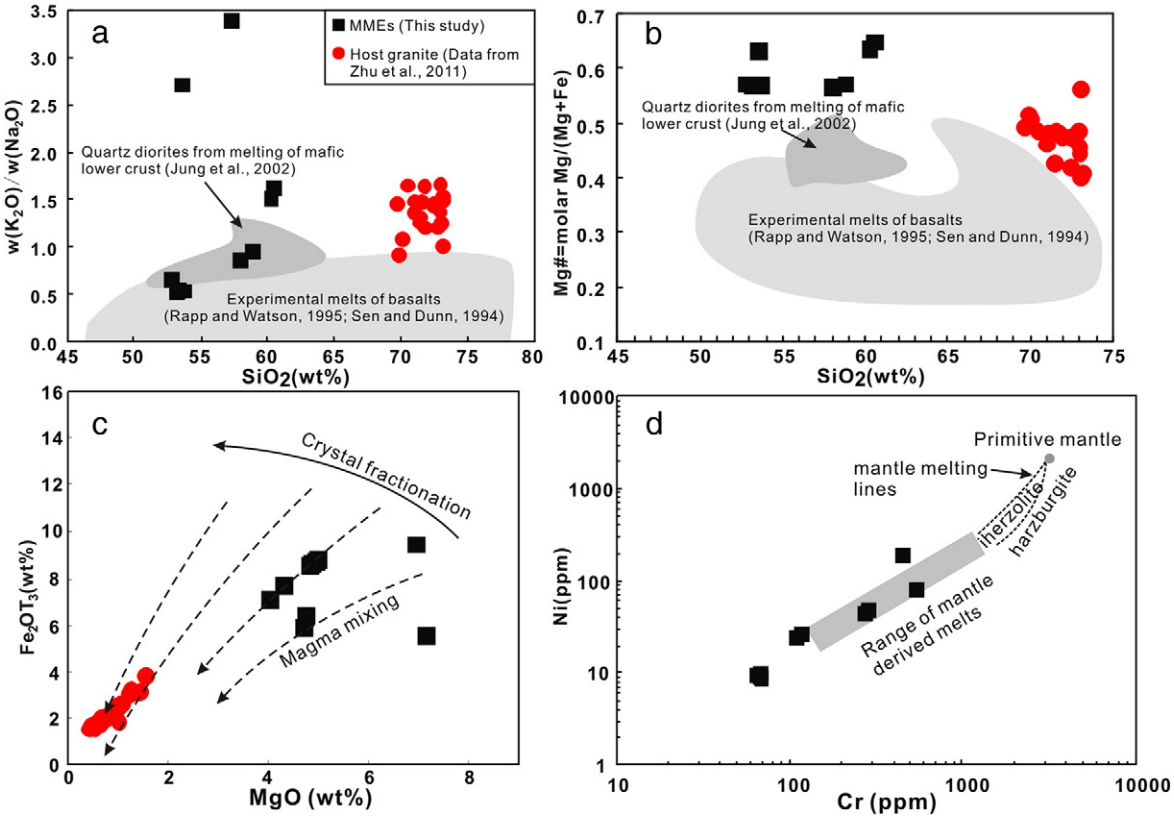

Fig. 15. Diagrams of SiO_2 vs. K_2O/Na_2O (a), SiO_2 vs. Mg# (Mg# = molar Mg / (Mg + Fe)) (b), Fe_2O_3T vs. MgO (c) (after Zorpi et al., 1989) for the Wenquan MMEs and host granite, and Ni vs. Cr diagram (d) for the MMEs (the mantle-derived melts are from Tsuchiya et al., 2005).

magmas. Existence of the zircons with positive $\varepsilon_{Hf(t)}$ values in the granite (Supplementary Table S2; Fig. 16) means that the granite was unlikely to be derived from pure crustal melts, instead, some high $\varepsilon_{Hf(t)}$ materials must have been involved. Hence, we could interpret the relatively high Mg# number of the granite (Fig. 15b) with some zircon positive $\varepsilon_{Hf(t)}$ values to be related to the incorporation of the mantle-derived magma through hybridization. Therefore, the coeval mafic magma was intimately involved in the generation of the felsic magma, not only providing thermal energy for crustal melting, but also mixing with the anatectic melts (Kistler et al., 1986; Dorais et al., 1990; Barbarin, 2005).

Putting together all the data including petrology, major-trace elements geochemistry, zircon U–Pb ages and heterogeneous Hf isotopes of the MMEs and the Wenquan granite, we suggest that the MMEs were mainly formed by partial melting of the Neoproterozoic SCLM, followed by crustal contamination. When the mafic magma intruded the lower continental crust, a thermal anomaly occurred, causing dehydration melting of the Neo-Mesoproterozoic crust, and subsequently generating the granitic melt from which the zircons crystallized with a wide variation of Hf isotopic composition. Meanwhile, sulfur and metals were transferred in a rather direct fashion from mafic to felsic magma as a result of magma mixing. The hybrid magma played an essential role in the generation of the Mo mineralization in the Wenquan pluton.

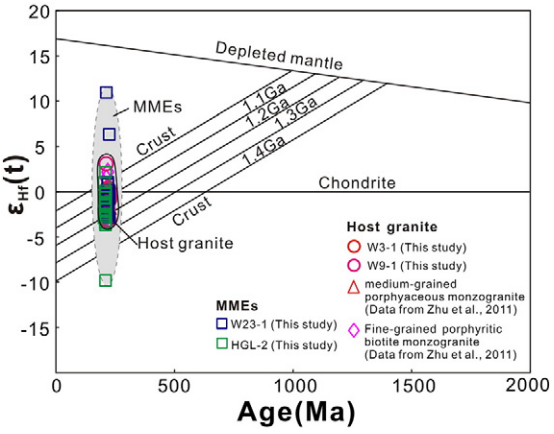

Fig. 16. Plot of zircon $\varepsilon_{Hf(t)}$ values vs. U–Pb ages for host granite and MMEs from the Wenquan pluton.

7.4. Geodynamic setting and genesis of ore deposit

All the ages obtained from molybdenite, granite and MMEs in this study are consistently Late Triassic, identical to the molybdenite Re–Os isochron age of 214 ± 7.1 Ma (MSWD = 0.77) and LA-ICP-MS zircon U–Pb ages of 216 ± 1.7 Ma and 217 ± 2 .0 Ma for the granite formerly measured by Zhu et al. (2009, 2011). The coherent ages suggest that the magma mixing processes and the Mo mineralization occurred contemporaneously in the Late Triassic. In addition, the Wenquan pluton has identical crystallization ages to the Late Triassic granites in the Qinling Orogen (Sun et al., 2002; Zhang et al., 2006, 2007; Gong et al., 2009a, b; Qin et al., 2009, 2010).

However, because of the divergent petrological and geochemical affinities shown by the Triassic granitoids dated from 248 to 200 Ma (Li et al., 2015), the following debated ideas regarding their tectonic setting are proposed: (1) Transition from a subduction-related magmatic arc to a post-collisional extension setting (Jiang et al., 2010; Liu et al., 2011; Dong et al., 2012); (2) A continental arc developed with the northward subduction of the Mianlue oceanic plate (Li et al., 2007; Chen, 2010; Chen and Santosh, 2014; Chen et al., 2014; Han et al., 2014; Mao et al., 2014; Li et al., 2015); and (3) The transitional setting from compression to extension regime (Li et al., 1996; Lu et al., 1996; Zhang et al., 2001; B.R. Zhang et al., 2002; Zhang et al., 2005; Qin et al., 2009, 2010; Zhu

et al., 2010, 2011, 2013). Among all the three, the third one is more favorable. The reason for this is that the Wenquan granite obviously belongs to the collisional granite, whose age data can be compared with both the syn-collisional granites with the ages of 205–220 Ma and the post-collisional granites having ages of 220–214 Ma in South Qinling (Ames et al., 1993; Li et al., 1993a, 1996; Lu et al., 1996; Hacker et al., 1998; Sun et al., 2002; Zheng et al., 2003; Zhang et al., 2005; Yang et al., 2006; Wang et al., 2007; Liu et al., 2008; Zeng et al., 2014). The formation of the Wenquan granite reflects the tectonic setting from compression to extension regime.

Generally, a collisional orogeny includes three stages: the early shortening, the shortening-extension transition and the late extension (Leech, 2001; Chen et al., 2007; Yang et al., 2014). During the transition from the collisional shortening to extension, the geothermal gradient is elevating due to the orogenic decompression, which enhances partial melting and fluid movement and further induces magmatism and fluid effect with high water content and oxygen fugacities (Sillitoe, 2010), and in turn creates a favorable condition for petrogenesis and mineralization (Vanderhaeghe and Teyssier, 2001; Chen et al., 2007; Yang et al., 2010, 2014; L.C. Zhang et al., 2009). Based on the comparison of the typical porphyry Mo–Cu deposits globally, Qiu et al. (2014) recognized that the tectonic transition setting are in particular a favorable metallogenic environment for the formation of porphyry Mo–Cu deposits. Considering the Qinling Orogen which experienced the late Indosinian post-collisional magmatism (189 Ma, Dong et al., 2012; 225 to 185 Ma, Wang et al., 2013; 225 to 205 Ma, Huang et al., 2013), we strongly suggest that the mineralization of the Wenquan Mo deposit occurred during the transition of tectonic regime from the syn-collision to post-collision.

The ~220 Ma magma mixing and emplacement of the Wenquan granite and MMEs represent products of the Late Triassic tectono-magmatic event. The Triassic collision along the Mianlue suture led to the south-directed thrust imbrication inside the Qinling–Dabie orogen, as a result, the crust thickening was up to 50 km (Zhang et al., 2001; Zhang et al., 2005). Sun et al. (2002) proposed a slab break-off model for the genesis of the widespread Triassic granitic magmatism in the WQO. According to geophysical data, a local asthenospheric upwelling caused a thermal pulse along the Mianlue suture. This thermal pulse beneath the thickened continental crust of the Qinling Orogen could result in the syn-collisional magmatism in response to the slab break-off from the buoyant continental lithosphere during subduction (Qin et al., 2009). Under such a condition, a model to illustrate the genesis and geodynamic setting of the Wenquan granite and associated Mo deposit is proposed (Fig. 17). The Wenquan granite was formed in the stage of syn- to post-collision transition during the collision orogeny between the South Qinling and the SCB along the Mianlue suture following the closure of the Qinling ocean in the Late Triassic (Zhang et al., 2001, 2004). The break-off of the subducted SCB lithosphere initiated an upwelling thermal pulse, which in turn initiated partial melting of the Neoproterozoic SCLM and the Neo-Mesoproterozoic lower crust. The processes finally resulted in the generation of mafic and granitic magmas, respectively. The mafic magma intruded the lower crust and interacted with granitic magma, which gave birth to the Mo-bearing granitic pluton containing MMEs. The ore-forming fluid was generated during the late aqueous and volatile-rich phase of magma crystallization stage in the Late Triassic, subsequently filled in the joints and cracks to form the Wenquan Mo deposit.

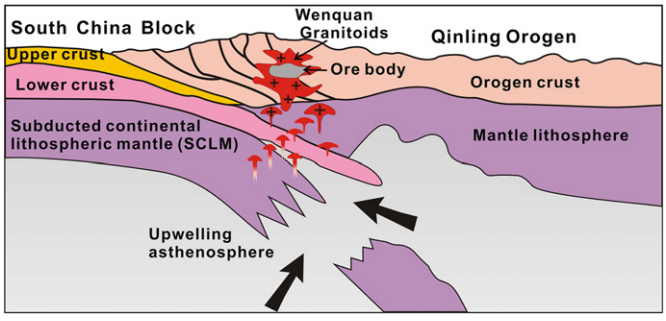

Fig. 17. Tectonic setting and dynamics of the Late Triassic Wenquan porphyry and related Mo deposit. For explanation see text.

8. Conclusions

(1) The Wenquan porphyry-type Mo deposit is hosted in the Wenquan granite. Three generations of mineral assemblage for the deposit are identified, of which the quartz–sulfide assemblage has played a major role in the Mo mineralization.
(2) Pb isotope study indicates that the granitic magma to form the Wenquan pluton was sourced from the middle-lower crust of the SCB, while the ore-forming materials incorporated the hydrothermal fluid differentiated from the Triassic magmatic system with minor contribution of the sedimentary country rock.
(3) The MMEs contained in the Wenquan granite were products of the mixing processes between the Late Mesoproterozoic crust-derived component and the Neoproterozoic SCLM-derived mafic materials, which made the Mo mineralization endowing in the Wenquan pluton possible.
(4) The age data from the Wenquan granite, MMEs and Molybdenite are consistently of Late Triassic (219–217 Ma). This means that the formation of the pluton by magmatic mixture and the Mo mineralization are contemporaneous, which occurred during the transition of tectonic regime from syn- to post-collision in the Qinling Orogen in the Late Triassic.

Supplementary data to this article can be found online at http://dx.doi.org/10.1016/j.gr.2015.09.013.

Acknowledgments

This study was jointly supported by the National Natural Science Foundation of China (Grant Nos. 41272092, 41421002, 41072068 and 41373064), Program for Changjiang Scholars and Innovative Research Team in University (Grant IRT1281), Natural Science Basic Research Program of Shaanxi Province, China (Grant No. 2013JZ013) and Graduate Innovation Funds of Northwest University, China (Grant No. YZZ12006). The authors express their appreciation for the handling work and thoughtful improvement of this manuscript by Profs. Yunpeng Dong and M. Santosh. We are grateful to three anonymous reviewers for their constructive comments that significantly improved the manuscript. Thanks are also given to Ms. Chunlei Zong for her assistance in lead isotopic analysis.

References

Ames, L., Tilton, G.R., Zhou, G.Z., 1993. Timing of collision of the Sino-Korean and Yangtse cratons: U–Pb zircon dating of coesite-bearing eclogites. Geology 21, 339–342.
Andersen, T., 2002. Correction of common lead in U–Pb analyses that do not report ^{204}Pb. Chemical Geology 192, 59–79.
Audetat, A., Pettke, T., 2006. Evolution of a porphyry-Cu mineralized magma system at Santa Rita, New Mexico (USA). Journal of Petrology 47, 2021–2046.
Barbarin, B., 2005. Mafic magmatic enclaves and mafic rocks associated with some granitoids of the central Sierra Nevada batholith, California: nature, origin, and relations with the hosts. Lithos 80, 155–177.
Barbarin, B., Didier, J., 1992. Genesis and evolution of mafic microgranular enclaves through various type of interaction between coexisting felsic and mafic magmas. Earth Science 83, 145–153.
Bateman, R., 1993. Mineral disequilibria under the microscope. In: Bateman, R., Castro, A. (Eds.), Heterogeneities in Felsic Igneous Rock at Scales from Crystals to Plutons, Workshop Notes, pp. 4–7.
Blichert-Toft, J., Albaréde, F., 1997. The Lu–Hf isotope geochemistry of chondrites and the evolution of the mantle–crust system. Earth and Planetary Science Letters 148, 243–258.

Bonin, B., 2004. Do coeval mafic and felsic magmas in post-collisional to within-plate regimes necessarily imply two contrasting, mantle and crustal, sources? A review. Lithos 78, 1–24.
Browne, B.L., Eichelberger, J.C., Patino, L.C., Vogel, T.A., Uto, K., Hoshizumi, H., 2006. Magma mingling as indicated by texture and Sr/Ba ratios of plagioclase phenocrysts from Unzen volcano, SW Japan. Journal of Volcanology and Geothermal Research 151, 103–116.
Burnham, C.W., 1997. Magmas and hydrothermal fluids. In: Barnes, H.L. (Ed.), Geochemistry of Hydrothermal Ore Deposits, 3rd edition John Wiley and Sons, New York, pp. 63–123.
Cameron, E.M., 1989. Scouring of gold from the lower crust. Geology 17, 26–29.
Cao, D.H., Wang, A.J., Li, W.C., Wang, G.S., Li, R.P., Li, Y.K., 2009. Magma mixing in the Pulang porphyry copper deposit: evidence from petrology and element geochemistry. Acta Geologica Sinica 83, 166–175 (in Chinese with English abstract).
Cao, X.F., Lv, X.B., Yao, S.Z., Mei, W., Zou, X.Y., Chen, C., Liu, S.T., Zhang, P., Su, Y.Y., Zhang, B., 2011. LA-ICP-MS U–Pb zircon geochronology, geochemistry and kinetics of the Wenquan ore-bearing granites from West Qinling, China. Ore Geology Reviews 43, 120–131.
Carten, R.B., White, W.H., Stein, H.J., 1993. High-grade granite related molybdenum system: classification and origin. In: Kirkham, R.V., Sinclair, W.D., Thorpe, R.I., Duke, J.M. (Eds.), Mineral Deposit Modeling. Geological Association of Canada Special Paper 40, pp. 521–554.
Chappell, B.W., White, A.J.R., 1992. I- and S-type granites in the Lachlan Fold Belt. Transactions of the Royal Society of Edinburgh: Earth Sciences 83, 1–26.
Chappell, B.W., White, A.J.R., Wyborn, D., 1987. The importance of residual source material (restite) in granite petrogenesis. Journal of Petrology 28, 1111–1138.
Chen, Y.J., 2010. Indosinian tectonic setting, magmatism and metallogenesis in Qinling Orogen, central China. Geology in China 37, 854–865 (in Chinese with English abstract).
Chen, Y.J., Santosh, M., 2014. Triassic tectonics and mineral systems in the Qinling Orogen, central China. Geological Journal 49, 338–358.
Chen, Y.J., Chen, H.Y., Zaw, K., Pirajno, F., Zhang, Z.J., 2007. Geodynamic settings and tectonic model of skarn gold deposits in China: an overview. Ore Geology Reviews 31, 139–169.
Chen, Y.J., Pirajno, F., Li, N., Guo, D.S., Lai, Y., 2009. Isotope systematics and fluid inclusion studies of the Qiyugou breccia pipe-hosted gold deposit, Qinling Orogen, Henan province, China: implications for ore genesis. Ore Geology Reviews 35, 245–261.
Chen, Y.J., Santosh, M., Somerville, I., Chen, H.Y., 2014. Indosinian tectonics and mineral systems in China: an introduction. Geological Journal 49, 331–338.
Chiaradia, M., Ulianov, A., Kouzmanov, K., Beate, B., 2012. Why large porphyry Cu deposit like Sr/Y magmas? Scientific Reports 2, 685.
Chu, N.C., Taylor, R.N., Chavagnac, V., Nesbitt, R.W., Boella, R.M., Milton, J.A., German, C.R., Bayonet, G., Burton, K., 2002. Hf isotope ratio analysis using multi-collector inductively coupled plasma mass spectrometry: an evaluation of isobaric interference corrections. Journal of Analytical Atomic Spectrometry 17, 1567–1574.
Collins, W.J., 1998. Evaluation of petrogenetic models for Lachlan Fold Belt granites: implications for crustal architecture and tectonic model. Australian Journal of Science 45, 483–500.
DeBievre, P., Taylor, P.D.P., 1993. Table of the isotopic composition of the elements. International Journal of Mass Spectrometry and Ion Processes 123, 149–166.
Didier, D., Barbarin, B., 1991. Enclaves and Granite Petrology, Developments in Petrology. Elsevier Science Publications, Amsterdam, pp. 1–625.
Dong, Y.P., Santosh, M., 2015. Tectonic architecture and multiple orogeny of the Qinling Orogenic Belt, Central China. Gondwana Research. http://dx.doi.org/10.1016/j.gr.2015.06.009.
Dong, Y.P., Yang, Z., Zhang, G.W., Zhao, X., Xu, J.G., Yao, A.P., 2008. Geochemistry of the ophiolite in the Guanzizhen area, west Qinling and its tectonic implications. Acta Geologica Sinica 82, 1186–1194 (in Chinese with English abstract).
Dong, Y.P., Genser, J., Neubauer, F., Zhang, G.W., Liu, X.M., Yang, Z., Heberer, B., 2011a. U–Pb and $^{40}Ar/^{39}Ar$ geochronological constraints on the exhumation history of the North Qinling terrane, China. Gondwana Research 19, 881–893.
Dong, Y.P., Zhang, G.W., Hauzenberger, C., Neubauer, F., Yang, Z., Liu, X.M., 2011b. Palaeozoic tectonics and evolutionary history of the Qinling orogen: evidence from geochemistry and geochronology of ophiolite and related volcanic rocks. Lithos 122, 39–56.
Dong, Y.P., Liu, X.M., Zhang, G.W., Chen, Q., Zhang, X.N., Li, W., Yang, C., 2012. Triassic diorites and granitoids in the Foping area: constraints on the conversion from subduction to collision in the Qinling orogen, China. Journal of Asian Earth Sciences 47, 123–142.
Dong, Y.P., Liu, X.M., Neubauer, F., Zhang, G.W., Tao, N., Zhang, Y.G., Zhang, X.N., Li, W., 2013. Timing of Paleozoic amalgamation between the North China and South China Blocks: evidence from detrital zircon U–Pb ages. Tectonophysics 586, 173–191.
Dorais, M.J., Whitney, J.A., Roden, M.F., 1990. Origin of mafic enclaves in the Dinkey Creek Pluton, Central Sierra Nevada batholith, California. Journal of Petrology 31, 853–881.
Du, A.D., Wu, S.Q., Sun, D.Z., Wang, S.X., Qu, W.J., Markey, R., Stein, H., Morgan, J., Malinovskiy, D., 2004a. Preparation and certification of Re–Os dating reference materials: molybdenite HLP and JDC. Geostandard and Geoanalytical Research 28, 41–52.
Du, Y.S., Qin, X.L., Tian, S.H., 2004b. Mesozoic magmatic to hydrothermal process in the Tongguanshan ore field, Tongling, Anhui Province, China: evidence from xenoliths and their hosts. Acta Petrologica Sinica 20, 339–350 (in Chinese with English abstract).
Eichelberger, J., 1980. Vesiculation of mafic magma during replenishment of silicic magma reservoirs. Nature 446–450.
Elburg, M., Vroon, P., Wagt, B., Tchalikian, A., 2005. Sr and Pb isotopic composition of five USGS glasses (BHVO-2G, BIR-1G, BCR-2G, TB-1G, NKT-1G). Chemical Geology 223, 196–207.
Elhlou, S., Belousova, E., Griffin, W.L., Pearson, N.J., O'Reilly, S.Y., 2006. Trace element and isotopic composition of GJ red zircon standard by laser ablation. Geochimica et Cosmochimica Acta 70, A158.
Feng, Y.M., Cao, X.D., Zhang, E.P., Hu, Y.X., 2002. The Structure, Orogenic Process and Geodynamics of the West Qinling Orogenic Belt. Map Publishing House, Xi'an, pp. 1–234 (in Chinese).
Foster, G., Lambert, D.D., Frick, L.R., Maas, R., 1996. Re–Os isotopic evidence for genesis of Archaean nickel ores from uncontaminated komatiites. Nature 382, 703–706.
Gong, H.J., Zhu, L.M., Sun, B.Y., Li, B., Guo, B., Wang, J.Q., 2009a. Zircon U–Pb ages and Hf isotopic composition of the Dongjiangkou granitic pluton and its mafic enclaves in the South Qinling terrain. Acta Petrologica Sinica 25, 3029–3042 (in Chinese with English abstract).
Gong, H.J., Zhu, L.M., Sun, B.Y., Li, B., Guo, B., 2009b. Zircon U–Pb ages and Hf isotope characteristics and their geological significance of the Shahewan, Caoping and Zhashui granitic plutons in the South Qinling orogen. Acta Petrologica Sinica 25, 248–264 (in Chinese with English abstract).
Guo, X.D., Ge, L.S., Wang, L., Wang, Z.H., Shi, X.C., 2012. Characteristics of deep-derived enclaves and its zircon LA-ICP-MS U–Pb age of Machangjing complex, Yunnan Province. Acta Petrologica Sinica 28, 1413–1424 (in Chinese with English abstract).
Hacker, R.B., Ratschbacher, L., Webb, L., 1998. U–Pb zircon ages constrain the architecture of the ultrahigh-pressure Qinling–Dabie Orogen, China. Earth and Planetary Science Letters 161, 215–230.
Halter, W.E., Pettke, T., Heinrich, C.A., 2002. The origin of Cu/Au ratios in porphyry-type ore deposits. Science 296, 1844–1846.
Halter, W.E., Bain, N., Becker, K., Heinrich, C.A., Landtwing, M., VonQuadt, A., Clark, A.H., Sasso, A.M., Bissig, T., Tosdal, R.M., 2004. From andesitic volcanism to the formation of a porphyry Cu–Au mineralizing magma chamber: the Farallón Negro Volcanic Complex, northwestern Argentina. Journal of Volcanology and Geothermal Research 136, 1–30.
Hamlyn, P.R., Keays, R.R., Cameron, W.E., Crawford, A.J., Waldron, H.M., 1985. Precious metals in magnesian low-Ti lavas: implications for metallogenesis and sulfur saturation in primary magmas. Geochimica et Cosmochimica Acta 49, 1797–1811.
Hanchar, J.M., Hoskin, P.W.O., 2003. Zircon. Reviews in Mineralogy and Geochemistry 53, 1–500.
Han, J.S., Yao, J.M., Chen, Y.J., 2014. Geochronology and geochemistry of the Dashui adakitic granitoids in the western Qinling Orogen, central China: implications for Triassic tectonic setting. Geological Journal 49, 383–401.
Harris, N.B.W., Pearce, J.A., Tindle, A.G., 1986. Geochemical characteristics of collision-zone magmatism. In: Coward, M.P., Ries, A.C. (Eds.), Collision Tectonics. Geological Society of London Special Publication vol. 19, pp. 67–82.
Hattori, K., Keith, J.D., 2001. Contribution of mafic melt to porphyry copper mineralization: evidence from Mount Pinatubo, Philippines, and Bingham Canyon, Utah, USA. Mineralium Deposita 36, 799–806.
Helz, R.T., 1976. Phase relations of basalts in their melting range at $P_{H_2O} = 5$ kbar. II melt compositions. Journal of Petrology 17, 139–193.
Huang, X.F., Mo, X.X., Yu, X.H., Li, X.W., Ding, Y., Wei, P., He, W.Y., 2013. Zircon U–Pb chronology, geochemistry of the Late Triassic acid volcanic rocks in Tanchang area, West Qinling and their geological significance. Acta Petrologica Sinica 29, 3968–3980 (in Chinese with English abstract).
Hu, S.X., Lin, Q.L., Chen, Z.M., Sheng, Z.L., Li, S.M., 1988. Geology and Mineralization Along the Collisional Belts Between the North China Block and South China Block. Nanjing Publishing House, Nanjing, pp. 1–558 (in Chinese).
Jackson, S.E., Pearson, N.J., Griffin, W.L., Belousova, W.A., 2004. The application of laser ablation-inductively coupled plasma-mass spectrometry to in situ U–Pb zircon geochronology. Chemical Geology 211, 47–69.
Jiang, Y.H., Jin, G.D., Liao, S.Y., Zhou, Q., Zhao, P., 2010. Geochemical and Sr–Nd–Hf isotopic constraints on the origin of late Triassic granitoids from the Qinling orogen, central China: implications for a continental arc to continent–continent collision. Lithos 117, 183–197.
Jung, S., Hoernes, S., Mezger, K., 2002. Synorogenic melting of mafic lower crust: constraints from geochronology, petrology and Sr, Nd, Pb and O isotope geochemistry of quartz diorites (Damara Orogen, Namibia). Contributions to Mineralogy and Petrology 143, 551–566.
Karsli, O., Chen, B., Aydin, F., Sen, C., 2007. Geochemical and Sr–Nd–Pb isotopic compositions of the Eocene Dölek and Sariçiçek Plutons, Eastern Turkey: implications for magma interaction in the genesis of high-K calc-alkaline granitoids in a post-collision extensional setting. Lithos 98, 67–96.
Keith, J.D., Whitney, J.A., Hattori, K., Ballantyne, G.H., Christiansen, E.H., Barr, D.L., Cannan, T.M., Hook, C.J., 1997. The role of magmatic sulfides and mafic alkaline magmas in the Bingham and Tintic Mining Districts, Utah. Journal of Petrology 38, 1679–1698.
Kelly, W.C., Rye, R.O., 1979. Geological, fluid inclusion and stable isotope studies of the tin–tungsten deposits of Panasqueira, Portugal. Economic Geology 74, 1721–1822.
Kemp, A.I.S., 2004. Petrology of high-Mg, low-Ti igneous rocks of the Glenelg River Complex (SE Australia) and the nature of their interaction with crustal melts. Lithos 78, 119–156.
Kinny, P.D., Maas, R., 2003. Lu–Hf and Sm–Nd isotope systems in zircon. In: Hanchar, J.M., Hoskin, P.W.O. (Eds.), Zircon. Reviews in Mineralogy and Geochemistry 53, pp. 327–341.
Kistler, R.W., Chappell, B.W., Peck, D.L., Bateman, P.C., 1986. Isotopic variation in the Tuolumne Intrusive Suite, central Sierra Nevada, California. Contributions to Mineralogy and Petrology 94, 205–220.
Leech, M.L., 2001. Arrested orogenic development: eclogitization delamination, and tectonic collapse. Earth and Planetary Science Letters 185, 149–159.
Li, S.G., Chen, Y., Cong, B.L., Zhang, Z., Zhang, R., Liou, D., Hart, S.R., Ge, N., 1993a. Collision of the North China and Yangtze blocks and formation of coesite-bearing eclogites: timing and processes. Chemical Geology 109, 70–89.

Li, X.Z., Yan, Z., Lu, X.X., 1993b. Granites of Qinling–Dabie Orogen. Geological Publishing House, Beijing, pp. 1–215 (in Chinese).
Li, S.G., Sun, W.D., Zhang, G.W., Chen, J.Y., Yang, Y.C., 1996. Chronology and geochemistry of metavolcanic rocks from Heigouxia Valley in the Mian–Lue tectonic zone, South Qinling: evidence for a Paleozoic oceanic basin and its close time. Science in China (Series D) 39, 300–310.
Li, Y.J., Ding, S., Chen, Y.B., Liu, Z.W., Dong, J.G., 2003a. New knowledge on the Wenquan granite in western Qinling. Geology and Mineral Resources of South China 3, 1–8 (in Chinese with English abstract).
Li, Y.J., Wang, R., Liu, Z.W., Liu, Z.B., Li, J.B., 2003b. Features and origin of mafic microgranular inclusions in the Mishuling intrusion in the West Qinling. Geological Bulletin of China 22, 506–511 (in Chinese with English abstract).
Li, N., Chen, Y.J., Zhang, H., Zhao, T.P., Deng, X.H., Wang, Y., Ni, Z.Y., 2007. Molybdenum deposits in East Qinling. Earth Science Frontiers 14, 186–198 (in Chinese with English abstract).
Li, N., Chen, Y.J., Santosh, M., Pirajno, F., 2015. Compositional polarity of Triassic granitoids in the Qinling Orogen, China: implication for termination of the northernmost paleo-Tethys. Gondwana Research 27, 244–257.
Liu, H.J., Chen, Y.J., Mao, S.D., Zhao, C.H., Yang, R.S., 2008. Element and Sr–Nb–Pb isotope geochemistry of ganite-porphyry dykes in the Yangshan gold belt, western Qinling Orogen. Acta Petrologica Sinica 24, 1101–1111 (in Chinese with English abstract).
Liu, S.W., Yang, P.T., Li, Q.G., Wang, Z.Q., Zhang, W.Y., Wang, W., 2011. Indosinian granitoids and orogenic process in the middle segment of the Qinling Orogen, China. Journal of Jilin University (Earth Science Edition) 41, 1928–1943 (in Chinese with English abstract).
Ludwig, K.R., 2003. User's Manual for Isoplot 3.0: A Geochronological Toolkit for Microsoft Excel. Berkeley Geochronology Center Special Publication, Berkeley, California, pp. 1–71.
Lu, X.X., Dong, Y., Chang, Q.L., Xiao, Q.H., Li, X.B., Wang, T., Zhang, G.W., 1996. Indosinian Shahewan rapakivi granite in Qinling and its dynamic significance. Science in China (Series D) 39, 266–272.
Mao, J.W., Zhang, Z.C., Zhang, Z.H., 1999. Re–Os isotopic dating of molybdenites in the Xiaoliugou W (Mo) deposit in the northern Qilian Mountains and its geological significance. Geochimica et Cosmochimica Acta 63, 1815–1818.
Mao, S.D., Chen, Y.J., Zhou, Z.J., Lu, Y.H., Guo, J.H., Qin, Y., Yu, J.Y., 2014. Zircon geochronology and Hf isotope geochemistry of the granitoids in the Yangshan gold field, western Qinling, China: implications for petrogenesis, ore genesis and tectonic setting. Geological Journal 49, 359–382.
Maughan, D.T., Keith, J.D., Christiansen, E.H., Pulsipher, T., Hattori, K., Evans, N.J., 2002. Contribution from mafic alkaline magmas to the Bingham porphyry Cu–Au–Mo deposit, Utah, USA. Mineralium Deposita 37, 17–37.
Ma, X.H., Chen, B., 2011. The source of hydrothermal fluids and mineralization in the Aolunhua porphyry Mo–Cu deposit, southern Da Hinggan Mountains: constraints from stable (C, H, O and S) and radiogenic (Pb) isotopes. Journal of Jilin University (Earth Science Edition) 41, 1770–1783 (in Chinese with English abstract).
Ma, X.H., Chen, B., Yang, M.C., 2013. Magma mixing origin for the Aolunhua porphyry related to Mo–Cu mineralization, eastern Central Asian Orogenic belt. Gondwana Research 24, 1152–1171.
Meng, Q.R., Zhang, G.W., 1999. Timing of collision of the North and South China blocks: controversy and reconciliation. Geology 27, 1–96.
Meng, J.X., Hou, Z.Q., Dong, G.Y., Liu, J.G., Qu, W.J., Yang, Z.S., Zuo, L.Y., Wan, L.J., Xiao, M.Z., 2007. The geological characteristics and Re–Os isotope age of molybdenite of the Xiongjiashan molybdenum deposit, Jiangxi Province. Acta Geologica Sinica 81, 946–950 (in Chinese with English abstract).
Middlemost, E.A.K., 1994. Naming materials in the magma/igneous rock system. Earth-Science Reviews 37, 215–224.
Mungall, J.E., 2002. Roasting the mantle: slab melting and the genesis of major Au and Au-rich Cu deposits. Geology 30, 915–918.
Ohmoto, H., 1972. Systematics of sulfur and carbon isotopes in hydrothermal ore deposits. Economic Geology 67, 551–579.
Perugini, D., Poli, G., Christofides, G., Eleftheriadis, G., 2003. Magma mixing in the Sithonia Plutonic Complex, Greece: evidence from mafic microgranular enclaves. Mineralogy and Petrology 78, 173–200.
Perugini, D., Ventura, G., Petrelli, M., Poli, G., 2004. Kinematic significance of morphological structures generated by mixing of magmas: a case study from Salina Island (southern Italy). Earth and Planetary Science Letters 222, 1051–1066.
Petford, N., Gallagher, K., 2001. Partial melting of mafic (amphibolitic) lower crust by periodic influx of basaltic magma. Earth and Planetary Science Letters 193, 483–499.
Qi, L., Hu, J., Gregoire, D.C., 2000. Determination of trace elements in granites by inductively coupled plasma mass spectrometry. Talanta 51, 507–513.
Qi, L., Zhou, M.F., Gao, J.F., Zhao, Z., 2010. An improved Carius tube technique for determination of low concentrations of Re and Os in pyrites. Journal of Analytical Atomic Spectrometry 25, 585–589.
Qin, J.F., Lai, S.C., Rodney, G., Diwu, C.R., Ju, Y.J., Li, Y.F., 2009. Geochemical evidence for origin of magma mixing for the Triassic monzonitic granite and its enclaves at Mishuling in the Qinling orogen (central China). Lithos 112, 259–276.
Qin, J.F., Lai, S.C., Diwu, C.R., Ju, Y.J., Li, Y.F., 2010. Magma mixing origin for the post-collisional adakitic monzogranite of the Triassic Yangba pluton, Northwestern margin of the South China block: geochemistry, Sr–Nd isotopic, zircon U–Pb dating and Hf isotopic evidences. Contributions to Mineralogy and Petrology 159, 389–409.
Qiu, K.F., Li, N., Taylor, R.D., Song, Y.H., Song, K.R., Han, W.Z., Zhang, D.X., 2014. Timing and duration of metallogeny of the Wenquan deposit in the West Qinling, and its constrain on a proposed classification for porphyry molybdenum deposits. Acta Petrologica Sinica 30, 2631–2643 (in Chinese with English abstract).
Raith, J.G., Stein, H.J., 2000. Re–Os dating and sulfur isotope composition of molybdenite from tungsten deposits in western Namaqualand, South Africa: implication for ore genesis and the timing of metamorphism. Mineralium Deposita 35, 741–753.
Rapp, R.P., Watson, E.B., 1995. Dehydration melting of metabasalt at 8–32 kbar: implications for continental growth and crust–mantle recycling. Journal of Petrology 36, 891–931.
Rapp, R.P., Watson, E.B., Miller, C.F., 1991. Partial melting of amphibolite/eclogite and the origin of Archean trondhjemites and tonalites. Precambrian Research 51, 1–25.
Ratschbacher, L., Hacker, B.R., Calvert, A., Webb, L.E., Crimmer, J.C., McWilliams, M.O., Ireland, T., Dong, S., Hu, J., 2003. Tectonics of the Qinling (central China): tectonostratigraphy, geochronology, and deformation history. Tectonophysics 366, 1–53.
Ren, X.H., 2009. Geological characteristics and genesis of molybdenum deposits in Wushan County of Gansu. Gansu Metallurgy 31, 58–62 (in Chinese with English abstract).
Richards, J.P., 2011. High Sr/Y magmas and porphyry Cu ± Mo ± Au deposits: just add water. Economic Geology 106, 1075–1081.
Roberts, M.P., Clemens, J.D., 1993. Origin of high-potassium, calc-alkaline, I-type granitoids. Geology 21, 825–828.
Robinson, B.W., Kusakabe, M., 1975. Quantitative preparation of sulfur dioxide for $^{32}S/^{34}S$ analyses from sulfides by combustion with cuprous oxide. Analytic Chemistry 47, 1179–1181.
Rollinson, H.R., 1993. Using Geochemical Data: Evaluation, Presentation, Interpretation. Longman Scientific and Technical Press, pp. 306–308.
Rudnick, R.L., Gao, S., 2003. Composition of the continental crust. In: Rudnick, R.L., Holland, H.D., Turekian, K.K. (Eds.), Treatise on Geochemistry vol. 3. Elsevier-Pergamon, Oxford, pp. 1–64.
Schidlowski, M., 1998. Beginning of terrestrial life: problems of the early record and implications for extraterrestrial scenarios. Instruments, methods, and missions for astrobiology. SPIE 3441, 149–157.
Sen, C., Dunn, T., 1994. Dehydration melting of a basaltic composition amphibolite at 1.5 and 2.0 GPa: implications for the origin of adakites. Contributions to Mineralogy and Petrology 117, 394–409.
Sillitoe, R.H., 1997. Characteristic and controls of the largest porphyry copper–gold and epithermal gold deposits in the circum-Pacific region. Australian Journal of Earth Sciences 44, 373–388.
Sillitoe, R.H., 2010. Porphyry copper systems. Economic Geology 105, 3–41.
Smoliar, M.I., Warker, R.J., Morgan, J.W., 1996. Re–Os ages of group IIA, IIIA, IVA and VIB iron meteorites. Science 271, 1099–1102.
Söderlund, U., Patchett, P.J., Vervoort, J.D., Isachsen, C.E., 2004. The ^{176}Lu decay constant determined by Lu–Hf and U–Pb isotope systematics of Precambrian mafic intrusions. Earth and Planetary Science Letters 219, 311–324.
Sparks, S.R.J., Marshall, L.A., 1986. Thermal and mechanical constraints on mixing between mafic and silicic magmas. Journal of Volcanology and Geothermal Research 29, 99–124.
Stern, C.R., Funk, J.A., Skewes, M.A., Arévalo, A., 2007. Magmatic anhydrite in plutonic rocks at the EL Teniente Cu–Mo deposit, Chile, and the role of sulfur- and copper-rich magmas in its formation. Economic Geology 102, 1335–1344.
Sun, S.S., McDonough, W.F., 1989. Chemical and isotopic systematics of oceanic basalts: implications for mantle composition and processes. In: Saunders, A.D., Norry, M.J. (Eds.), Magmatism in the Ocean Basins. Geological Society of London Special Publications 42, pp. 313–345.
Sun, W.D., Li, S.G., Chen, Y.D., Li, Y.J., 2002. Timing of synorogenic granitoids in the south Qinling, central China: constraints on the evolution of the Qinling–Dabie Orogenic Belt. Journal of Geology 110, 457–468.
Taylor, S.R., McLennan, S.M., 1995. The geochemical evolution of the continental crust. Review in Geophysics 33, 241–265.
Tsuchiya, N., Suzuki, S., Kimura, J.I., Kagami, H., 2005. Evidence for slab melt/mantle reaction: petrogenesis of Early Cretaceous and Eocene high-Mg andesites from the Kitakami Mountains, Japan. Lithos 79, 179–206.
Vanderhaeghe, O., Teyssier, C., 2001. Partial melting and flow of orogens. Tectonophysics 342, 451–472.
Vernon, R.H., 1984. Microgranitoid enclaves: globules of hybrid magma quenched in a plutonic environment. Nature 304, 438–439.
Vernon, R.H., Etheridge, M.E., Wall, V.J., 1988. Shape and microstructure of microgranitoid enclaves: indicators of magma mingling and flow. Lithos 22, 1–11.
Vervoort, J.D., Blichert-Toft, J., 1999. Evolution of the depleted mantle: Hf isotope evidence from juvenile rocks through time. Geochimica et Cosmochimica Acta 63, 533–556.
Waight, T.E., Maas, R., Nicholls, I.A., 2000. Fingerprinting feldspar phenocrysts using crystal isotopic composition stratigraphy: implications for crystal transfer and magma mingling in S-type granites. Contributions to Mineralogy and Petrology 139, 227–239.
Wang, X.X., Wang, T., Jahn, B.M., Hu, N.G., Chen, W., 2007. Tectonic significance of Late Triassic post-collisional lamprophyre dykes from the Qinling Mountains (China). Geological Magazine 144, 837–848.
Wang, F., Zhu, L.M., Guo, B., Yang, T., Luo, Z.Z., 2012. Geological and geochemical characteristics of the Wenquan molybdenum deposit and ore-forming process in the western Qinling. Geology and Exploration 48, 0713–0727 (in Chinese with English abstract).
Wang, X.X., Wang, T., Zhang, C.L., 2013. Neoproterozoic, Paleozoic, and Mesozoic granitoid magmatism in the Qinling Orogen, China: constraints on orogenic process. Journal of Asian Earth Sciences 72, 129–151.
Weinberg, R.F., Sial, A.N., Pessoa, R.R., 2001. Magma flow within the Tavares pluton, northeastern Brazil: compositional and thermal convection. Geological Society of America Bulletin 113, 508–520.
Wiebe, R.A., Smith, D., Sturm, M., King, E.M., Seckler, M.S., 1997. Enclaves in the Cadillac Mountain granite (coastal Maine): samples of hybrid magma from the base of the chamber. Journal of Petrology 38, 393–423.
Wiedenbeck, M., Griffin, W.L., 1995. Three natural zircon standards for U–Th–Pb, Lu–Hf, trace element and REE analyses. Geostandards Newsletter 19, 1–23.

Wiedenbeck, M., Hanchar, J.M., Peck, W.H., Sylvester, P., Valley, J., Whitehouse, M., Kronz, A., Morishita, Y., Nasdala, L., 2004. Further characterization of the 91500 zircon crystal. Geostandards and Geoanalytical Research 28, 9–39.
Wolf, M.B., Wyllie, P.J., 1994. Dehydration melting of amphibolite at 10 kbar: the effects of temperature and time. Contributions to Mineralogy and Petrology 115, 369–383.
Woodhead, J.D., Hergt, J., Shelley, M., Eggins, S., Kemp, R., 2004. Zircon Hf-isotope analysis with an excimer laser, depth profiling, ablation of complex geometries, and concomitant age estimation. Chemical Geology 209, 121–135.
Yang, J.H., Wu, F.Y., Chung, S.L., Wilde, S.A., Chu, M.F., 2006. A hybrid origin for the Qianshan A-type granite, northeast China: geochemical and Sr–Nd–Hf isotopic evidence. Lithos 89, 89–106.
Yang, J.H., Wu, F.Y., Wilde, S.A., Xie, L.W., Yang, Y.H., Liu, X.M., 2007. Tracing magma mixing in granite genesis: in situ U–Pb dating and Hf-isotope analysis of zircons. Contributions to Mineralogy and Petrology 153, 177–190.
Yang, Z.M., Hou, Z.Q., Song, Y.C., Li, Z.Q., Xia, D.X., Pan, F.C., 2008. Qulong superlarge porphyry Cu deposit in Tibet: geology, alteration and mineralization. Mineral Deposit 27, 279–318 (in Chinese with English abstract).
Yang, L.Q., Liu, J.T., Zhang, C., Wang, Q.F., Ge, L.S., Wang, Z.L., Zhang, J., Gong, Q.J., 2010. Superimposed orogenesis and metallogenesis: an example from the orogenic gold deposits in Ailaoshan gold belt, Southwest China. Acta Petrologic Sinica 26, 1723–1739 (in Chinese with English abstract).
Yang, T., Zhu, L.M., Wang, F., Gong, H.J., Lu, R.K., 2013. Geochemistry, petrogenesis and tectonic implications of the granitic plutons at the Liziyuan orogenic gold deposit in Western Qinling Orogen, China. Geological Magazine 150, 50–71.
Yang, L.Q., Deng, J., Goldfarb, R.J., Zhang, J., Gao, B.F., Wang, Z.L., 2014. $^{40}Ar/^{39}Ar$ geochronological constraints on the formation of the Dayingezhuang gold deposit: new implications for timing and duration of hydrothermal activity in the Jiaodong gold province, China. Gondwana Research 25, 1469–1483.
Yuan, H.L., Gao, S., Liu, X.M., Li, H.M., Gunther, D., Wu, F.Y., 2004. Accurate U–Pb age and trace element determinations of zircon by laser ablation-inductively coupled plasma mass spectrometry. Geostandards Newsletter 28, 353–370.
Yuan, H.L., Gao, S., Dai, M.N., Zong, C.L., Günther, D., Fontaine, G.H., Liu, X.M., Diwu, C.R., 2008. Simultaneous determinations of U–Pb age, Hf isotopes and trace element compositions of zircon by excimer laser ablation quadrupole and multiple collector ICP-MS. Chemical Geology 247, 100–117.
Zartman, R.E., Doe, B.R., 1981. Plumbotectonics—the model. Tectonophysics 75, 135–142.
Zeng, Q.T., McCuaig, T.C., Tohver, E., Bagas, L., Lu, Y.J., 2014. Episodic Triassic magmatism in the western South Qinling Orogen, central China, and its implications. Geological Journal 49, 402–423.
Zhang, L.G., 1995. Block-geology of Eastern Asia Lithosphere—Isotope Geochemistry and Dynamics of Upper Mantle, Basement and Granite. Chinese Science Press, Beijing, pp. 1–252 (in Chinese with English abstract).
Zhang, G.W., Meng, Q.R., Lai, S.C., 1995. Tectonics and structure of the Qinling Orogenic belt. Science in China. Series B 38, 1379–1394 (in Chinese).
Zhang, G.W., Yu, Z.P., Dong, Y.P., Yao, A.P., 2000. On Precambrian framework and evolution of the Qinling belt. Acta Petrologica Sinica 16, 11–21 (in Chinese with English abstract).
Zhang, G.W., Zhang, B.R., Yuan, X.C., Xiao, Q.H., 2001. Qinling Orogen Belt and Continental Geodynamics. Science Press, Beijing, pp. 1–729 (in Chinese).
Zhang, B.R., Gao, S., Zhang, H.F., 2002a. Geochemistry of Qinling Orogen. Science Press, Beijing, pp. 1–187 (in Chinese with English abstract).
Zhang, J., Chen, Y.J., Shu, G.M., Zhang, F.X., Li, C., 2002b. Compositional study of minerals within the Qinlingliang granite, Southwestern Shaanxi Province and discussions on the related problems. Science in China (Series D) 45, 662–672.
Zhang, G.W., Dong, Y.P., Lai, S.C., 2004. Mianlue tectonic zone and Mianlue suture zone on southern margin of Qinling–Dabie orogenic belt. Science in China (Series D) 47, 300–316.
Zhang, C.L., Zhang, G.W., Yan, Y.X., Wang, Y., 2005. Origin and dynamic significance of Guangtoushan granitic plutons to the north of Mianlue zone in southern Qinling. Acta Petrologica Sinica 21, 711–720 (in Chinese with English abstract).
Zhang, H.F., Zhang, B.R., Harris, N., Zhang, L., Chen, Y.L., Chen, N.S., Zhao, Z.D., 2006. U–Pb zircon SHRIMP ages, geochemical and Sr–Nd–Pb isotopic compositions of intrusive rocks from the Longshan–Tianshui area in the Southeast corner of the Qilian orogenic belt, China: constraints on petrogenesis and tectonic affinity. Journal of Asian Earth Sciences 27, 751–764.
Zhang, H.F., Jin, L.L., Zhang, L., Harris, N., Zhou, L., Hu, S.H., Zhang, B.R., 2007. Geochemical and Pb–Sr–Nd isotopic compositions of granitoids from western Qinling belt: constraints on basement nature and tectonic affinity. Science in China (Series D) 50, 184–196.
Zhang, L.C., Wu, H.Y., Wan, B., Chen, Z.G., 2009a. Ages and geodynamic settings of Xilamulun Mo–Cu metallogenic belt in the northern part of the North China Craton. Gondwana Research 16, 243–254.
Zhang, Q., Yin, X.M., Yin, Y., Jin, W.J., Wang, Y.L., Zhao, Y.Q., 2009b. Issues on metallogenesis and prospecting of gold and copper deposits related to adakite and Himalayan type granite in west Qinling. Acta Petrologica Sinica 25, 3103–3122 (in Chinese with English abstract).
Zheng, Y.F., 2008. A perspective view on ultrahigh-pressure metamorphism and continental collision in the Dabie–Sulu orogenic belt. Chinese Science Bulletin 53, 3081–3104.
Zheng, Y.F., Fu, B., Gong, B., Li, L., 2003. Stable isotope geochemistry of ultrahigh pressure metamorphic rocks from the Dabie–Sulu orogen in China: implications for geodynamics and fluid regime. Earth Science Review 62, 105–161.
Zheng, Y.F., Zhao, Z.F., Wu, Y.B., Zhang, S.B., Liu, X.M., Wu, F.Y., 2006. Zircon U–Pb age, Hf and O isotope constraints on protolith origin of ultrahigh-pressure eclogite and gneiss in the Dabie orogen. Chemical Geology 231, 135–158.
Zheng, Y.F., Zhang, S.B., Zhao, Z.F., Wu, Y.B., Li, X.H., Li, Z.X., Wu, F.Y., 2007. Contrasting zircon Hf and O isotopes in the two episodes of Neoproterozoic granitoids in South China: implications for growth and reworking of continental crust. Lithos 96, 127–150.
Zheng, Y.F., Chen, R.X., Zhao, Z.F., 2009. Chemical geodynamics of continental subduction-zone metamorphism: insights from studies of the Chinese Continental Scientific Drilling (CCSD) core samples. Tectonophysics 475, 327–358.
Zheng, Y.F., Xiao, W.J., Zhao, G.C., 2013. Introduction to tectonics of China. Gondwana Research 23, 1189–1206.
Zhou, J.L., Han, H.T., 2010. Mineralization characteristics and alteration zoning of Wenquan molybdenum deposit in West Qinling. Global Geology 29, 248–255 (in Chinese with English abstract).
Zhu, B.Q., 1998. The Theory and Application of the Isotopic Systematic in Geoscience Concurrent Discussion of the Continental Crust and Mantle Evolvement in China. Science Publishing House, Beijing, pp. 1–330 (in Chinese with English abstract).
Zhu, L.M., Zhang, G.W., Guo, B., Li, B., 2008. U–Pb (LA-ICP-MS) zircon dating for the large Jinduicheng porphyry Mo deposit in the east Qinling, China, and its metallogenetic geodynamical setting. Acta Geologica Sinica 82, 204–220 (in Chinese with English abstract).
Zhu, L.M., Ding, Z.J., Yao, S.Z., Zhang, G.W., Song, S.G., Qu, W.J., Guo, B., Lee, B., 2009. Ore-forming event and geodynamic setting of molybdenum deposit at Wenquan in Gansu Province, Western Qinling. Chinese Science Bulletin 54, 2309–2324.
Zhu, L.M., Zhang, G.W., Lee, B., Guo, B., Gong, H.J., Kang, L., Lv, S.L., 2010. Zircon U–Pb dating and geochemical study of the Xianggou granite in the Ma'anqiao gold deposit and its relationship with gold mineralization. Science China Earth Sciences 53, 220–240.
Zhu, L.M., Zhang, G.W., Chen, Y.J., Ding, Z.J., Gong, H.J., Guo, B., Wang, F., Lee, B., 2011. Zircon U–Pb ages and geochemistry of the Wenquan Mo-bearing granitioids in Western Qinling, China: constraints on the geodynamic setting for the newly discovered Wenquan Mo deposit. Ore Geology Reviews 39, 46–62.
Zhu, L.M., Zhang, G.W., Yang, T., Wang, F., Gong, H.J., 2013. Geochronology, petrogenesis and tectonic implications of the Zhongchuan granitic pluton in the Western Qinling metallogenic belt, China. Geological Journal 48, 310–334.
Zorpi, M.J., Coulon, C., Orsini, J.B., Cocirta, C., 1989. Magma mingling, zoning and emplacement in calc-alkaline granitoid plutons. Tectonophysics 157, 315–329.